Terrestrial dominance of organic carbon in an Early Cretaceous syn-rift lake and its response to sequence evolution and paleoclimate change

Qianyou Wang [a], Yaohua Li [b,*], James E. P. Utley [a], Joe Gardner [a], Bei Liu [c], Jianfang Hu [d], Longyi Shao [e] Xin Wang [f], Fenglin Gao [g], Dadong Liu [f], Haibin Li [h], Zhenxue Jiang [f], Richard H. Worden [a,*]

[a] Department of Earth, Ocean and Ecological Sciences, University of Liverpool, Liverpool L69 3GP, UK; *Qianyou.Wang@liverpool.ac.uk* (Q.W.); *etrsi@liverpool.ac.uk* (J.U.); *Joseph.Gardner@liverpool.ac.uk* (J.G.)

[b] Oil and Gas Survey, China Geological Survey, Beijing 100083, China;

[c] School of Earth Resources, China University of Geosciences, Wuhan, Hubei 430074, China; *liubei12@cug.edu.cn*

[d] State Key Laboratory of Organic Geochemistry, Guangzhou Institute of Geochemistry, Chinese Academy of Sciences, Guangzhou 510640, China; *hujf@gig.ac.cn*

[e] College of Geoscience and Surveying Engineering, China University of Mining and Technology, Beijing 100083, China; ShaoL@cumtb.edu.cn

[f] State Key Laboratory of Petroleum Resources and Prospecting, China University of Petroleum (Beijing), Beijing 102249, China; *wangxin.geo@outlook.com* (X.W.); *liudd@cup.edu.cn* (D.L.); *jiangzx@cup.edu.cn* (Z.J.)

[g] Institute of Geomechanics, Chinese Academy of Geological Sciences, Beijing 100044, China; *gfenglin2020@126.com*

[h] Research Institute, Northeast Oil & Gas Branch of SINOPEC, Changchun 130062, China; *lihb@sinopec.com*

* Corresponding author: *lyaohua@mail.cgs.gov.cn* (Y.L.); *rworden@liverpool.ac.uk* (R.W.)

Abstract: Organic carbon (OC) burial in lakes can decrease atmospheric CO_2 level and regulate the climate over geological time. Abundant input of terrestrially-derived OC leads to high variability in the OC origin and type, but its role in determining organic-rich sediments tends to be overlooked in prior studies. Here, we investigated the OC source and concentration of the Lower Cretaceous (Middle Aptian to Lower Albian) Shahezi Formation (Songliao Basin, NE Asia) to reveal the burial of terrestrial OC in relation to syn-rift lake evolution and paleoclimate change. The sequence stratigraphic framework of fan-deltaic and lacustrine successions was established by identifying depositional facies and sequence boundaries. The lacustrine-dominated interval was further subdivided into four subfacies (i.e., lake shore to littoral beach bar, shallow-littoral, sublittoral, and profundal) and a few cyclic, parasequence-order packages, using 90 meters of continuous cores and high sampling frequency of RoqSCAN SEM-EDS. Multiple independent proxies (macerals under the correlative light and electron microscopy, pyrolysis indices, R_o, TOC/TN, and $\delta^{13}C_{org}$) suggest that the organic fraction of the highly mature shales and mudstones was predominantly contributed by terrestrially-derived OC (gas-prone Type III/IV kerogen). A direct correlation between subfacies ranks, chemical weathering proxies (CIA, CIA_{corr}, and $Ln(Al_2O_3/Na_2O)$), and OC burial (TOC and HI) reveals that terrestrial OC input displays a good response to lake base-level change and climate conditions. The steep syn-rift slope and subaqueous transport of OC-bearing sediments (e.g., matrix-supported pebbly mudstone), triggered by rapid subsidence and fault activities, may have promoted the high input of terrestrial OC. A comparison between time equivalent and terrestrial records from high and low paleolatitudes suggests that the shift from syn-rift to post-rift phase was accompanied by an increase in TOC concentration and a change toward type I kerogen of aquatic origin. The tectonic process of evolving rift basins might be an important forcing function for the change of OC sources and concentrations, which is responsible for the long-term OC burial in hinterland environments.

Keywords: black shale; organic carbon; lake; rift basin; paleoclimate; chemical weathering

1. INTRODUCTION

Lakes represent an important sink in the global terrestrial carbon cycle and therefore can regulate the climate over geologic timescales (Tranvik et al., 2009; Mendonça et al., 2017). Aquatic algae within the water column and land plants in the lake watershed generate organic carbon (OC) from atmospheric CO_2 through photosynthesis (Meyers and Ishiwatari, 1993; Meyers and Lallier-vergés, 1999; Fig. 1). A small fraction of this OC is transported and deposited onto the lake floor, buried in sediments, and transformed into fossil carbon (Schlünz and Schneider, 2000; Regnier et al., 2022). Extensive studies on marine rocks have identified that OC accumulation is controlled by interactions of three dominant variables in the depositional environments: organic production, destruction, and dilution (Pedersen and Calvert, 1990; Arthur and Sageman, 1994; Tyson, 2001; Bohacs et al., 2005; Katz, 2005; Tyson, 2005; Fig. 2); similar mechanisms are also valid for lake systems (Kelts, 1988; Katz, 1990; Katz, 1995). However, the lakes are not just small versions of oceans. There are many differences between marine and lacustrine systems, e.g., sediment and water input, base-level fluctuations, water circulations, and factors controlling primary productivity (Bohacs et al., 2000). Successful characterization of lacustrine OC burial requires us to integrate the three interrelated variables into the tectono-stratigraphic or climate frameworks (e.g., Harris et al., 2004; Hao et al., 2011; Harris and Tucker, 2015; Fig. 2).

Models about the tectonic and climatic controls on the lacustrine sequence development and OC accumulation have been well established for the modern lakes of the east African rift system (Katz, 1990), the Eocene Green River Formation of western United States (Carroll and Bohacs, 1999; Bohacs et al., 2000; Bohacs, 2002), the Newark Supergroup of eastern US (Olsen and Katz, 1990; Olsen et al., 1996), the Upper Permian Formations in the Junggar Basin of northwestern China (Carroll et al., 1992; Carroll, 1998), and the Early

Cretaceous successions in the Congo Basin of western Africa (Harris, 2000; Harris et al., 2004; Harris et al., 2005). Olsen and Katz (1990) suggested that the balance between water inflow and outflow (e.g., precipitation and evaporation) governs the depths and duration of lakes (Fig. 2). Lambiase (1990) and Katz (1995) suggested that lacustrine deposition and effective OC concentration can only occur in deep, sediment-starved basins formed by rapid subsidence and rift shoulders. Based on these models, three lake facies associations (i.e., evaporative, fluctuating profundal, fluvial-lacustrine) were determined by the shifting balance between tectonically-created accommodation and climatically-controlled fill by sediment and water (Carroll and Bohacs, 1999; Fig. 2). Three corresponding lake models integrating the depositional facies, stratal stacking patterns, lithologies, and sedimentary structures were established to predict the lake-type controls on the OC accumulation and petroleum source rock quality (Bohacs, 1998; Bohacs et al., 2000; Carroll and Bohacs, 2001).

The topography and geometry of the evolving rift basins play important roles in nutrient influx and organic production (Fig. 2). In this process, soil, ground water circulation, and river input have been proposed as key links for storing and transporting nutrients required for aquatic organism growth (Katz, 1995; Harris and Tucker, 2015). During the initial active phase of rift basins, bio-productivity largely depends on the external nutrient input as the internal nutrient recycling is weak (Dean, 1981; Katz, 1995). The high weathering rates triggered by tectonic uplift and the resulting steep slopes may introduce extensive mineral-derived nutrients into the photonic zone of rift basins, especially for the basins where the drainage area and surrounding terrane are dominated by phosphorites, carbonates, and volcanics (Katz, 1990; Katz, 1995; Harris et al., 2004). Although the lake rift phase with a low slope gradient generally corresponds to weak physical weathering intensity and decreased nutrients, more vegetation-derived OC might be stored in thickening soils and further converted to dissolved inorganic carbon and associated nutrients (Harris et al., 2004; Harris and Tucker, 2015). Paleoclimatic conditions, in conjunction with topographic depressions, also control the nature and level of organic production and preservation by determining the water availability and chemistry (Fig. 2). Organic-rich intervals are typically deposited in periods of high precipitation when the nutrient flux and primary productivity are increased due to enhanced chemical weathering and effective recycling of vegetation in drainage basins (Katz, 1990; Harris et al., 2005). Water chemistry contributes to the extent of OC degradation by altering water density, oxygen solubility and determining the availability of other chemical oxidizing agents (Katz, 1990).

Due to the wide variety of lakes in tectonic context, depositional settings, climate conditions, and hydrodynamic regimes, it is challenging to make generalizations concerning the ability of lakes to preserve OC from diverse sources (Powell, 1986). Despite the well-established OC enrichment models of lacustrine sediments with greater than 3% TOC values and predominantly aquatic organic matter (Tyson, 2005), the mechanisms responsible for the terrestrial dominance of OC in lacustrine shales remain controversial. Abundant input of land-derived organic materials leads to high variability in the OC origin and type, especially for the overfilled basins characterized by fluvial-lacustrine deposits and shoreline progradation (Bohacs, 1998; Bohacs et al., 2000). In some extreme cases, the organic fraction of lacustrine sediments is predominantly composed of terrigenous OC, which displays low to high OC enrichment (TOC = 0.05%–27.44%), low to moderate hydrogen indices (< 600 mg HC/g TOC), and high humic kerogen concentrations (Table 1). Prior geochemical studies suggested that the land plant-derived particles are prone to selected preservation, compared to aquatic organisms. For example, the low hydrogen indicies and gas-prone OC enrichment result from the oxidized water column (e.g., Lake Albert, Katz, 1990). Compared to aquatic algae, the allochthonous OC, with a small surface area-to-volume ratio, has a higher settling rate and shorter oxygen exposure time (Katz, 1995; Sobek et al., 2009). In addition, these less reactive and hydrogen-depleted materials are comparatively unsusceptible to microbial decomposition, diagenesis, and thermal maturation, whereas aquatic-derived macerals are generally not present after the peak oil window (Hackley and Cardott, 2016; Mastalerz et al., 2018; Liu et al., 2019a, 2022a; Sanei, 2020; Fig. 2). However, evidence from organic petrographic studies shows that the predominantly type III kerogen in some sections is derived from terrestrial sources other than degraded algae material (Table 1). The OC content and type display a strong dependence on tectonic activity and depositional setting (Katz, 1995; Harris et al., 2004; Hao et al., 2011). Thus, the currently available models are insufficient to explain the organic-rich lacustrine deposition dominated by terrestrial-derived OC. Although some provocative models exist for terrigenous OC input in the marine sequence stratigraphic and climatic context (Algeo et al., 2004; Liu et al., 2019b), it is unclear whether they are directly transferable to lacustrine settings because of the considerable differences in both temporal and volumetric scales of the two systems.

The continental rift Songliao Basin have been reported to comprise extensive deposits of lacustrine black shales and represent a nearly complete terrestrial depositional record of Cretaceous greenhouse climate formation (Wang et al., 2016). The Shahezi Formation is a thick epiclastic-pyroclastic succession from the maximum rifting phase of the Songliao Basin (Wang et al., 2016; Cai et al., 2017; Ji et al., 2019). Precise zircon U-Pb dating from International Continental Scientific Drilling Program (ICDP) SK-2 borehole shows that the Shahezi Formation was deposited from the Middle Aptian to Early Albian (118–111 Ma) (Yu et al., 2020; Liu et al., 2021). Visual microscopic examination of organic macerals suggested that the organic fraction of the Shahezi Formation shales is composed mainly of terrestrial-derived vitrinite and inertinite (Gao et al., 2018; Xu et al., 2022b). Its high thermal maturity and abrupt facies changes make it challenging to characterize the variation of OC source and composition. This paper presents the results of an integrated study utilizing approximately 90-meter cores of Shahezi Formation shales and mudstone recovered by JLYY1 borehole drilled by the China Geological Survey (Xu et al., 2020a; Wang et al., 2023). The goals of this study are: 1) to characterize the OC type and concentration of black mudstones; 2) to reveal the variation of OC source and content in relation to rift stratigraphic evolution and paleoclimate change. This study interprets the sources of OC deeply buried in highly mature rocks using multiple independent proxies, thus, helps to answer the question 'How accurately does the OC type in sediments reflect the original sources?'. A direct correlation between depositional settings, chemical weathering intensity, and terrigenous OC input is also established based on sedimentological and geochemical tests of high sampling frequency. As these insights also speak to the effectiveness of carbon burial in fine-grained sediments, this study may contribute to a better understanding of the global carbon cycle and Cretaceous climate change.

2. GEOLOGICAL SETTING

The Songliao Basin is one of several Mesozoic rift basins in the eastern segment of the Central Asian Orogenic Belt, flanked to the south by North China Craton (Fig. 3) (Wang et al., 2016; Meng et al., 2021). A series of Early Cretaceous rift basins near the west Pacific continental arc developed throughout the northeast Asia continent (Meng et al., 2021); these rift basins are typically ascribed to backarc extension induced by the westward subduction of the paleo-Pacific plate (Zhu et al., 2012a; Zhu et al., 2012b). The Songliao Basin is located between two Late Mesozoic active continental margins and evolved on a pre-Triassic basement (Wang et al., 2016).

The tectono-stratigraphic section in the Songliao Basin can be divided into three parts by three regional angular unconformities, including the basal unconformity (Fig. 3D) (Wang et al., 2016). (1) The syn-rift section corresponds to the Upper Jurassic–Lower Cretaceous Huoshiling (J_3h), Shahezi (K_1sh), and Yingcheng (K_1yc) Formations, which are characterized by widespread fault-limited grabens and epiclastic-pyroclastic successions. Age dating of the Shahezi Formation sequences (118–111 Ma) is constrained due to the abundant volcanic rocks datable by radiometric techniques, such as the underlying J_3h andesites (Wang et al., 2017a), K_1sh tuffites (Yu et al., 2020; Liu et al., 2021), and the overlying K_1yc rhyolites and basalts (Ji et al., 2019) (Fig. 3D). The subsidence rate reached its peak value of 173.8 m/Ma during the Shahezi Formation, which represents the most intense rifting stage of the creation of the Songliao Basin (Wang et al., 2016; Liu et al., 2021; Wang et al., 2021). (2) The post-rift section includes the Lower Cretaceous–Upper Cretaceous Denglouku (K_1d), Quantou (K_1q), Qingshankou (K_2qn), Yaojia (K_2y), and Nenjiang (K_2n) Formations, which are fluvial-deltaic-lacustrine sediments deposited during a period of reduced subsidence. (3) The structural inversion sequence consists of Upper Cretaceous Sifangtai (K_2s)

and Mingshui (K_2m) Formations, during which time the basin area reduced rapidly, and the depocenter migrated to the northwest (Feng et al., 2010; Wang et al., 2016) (Fig. 3D).

The Lishu Rift Depression located in the southeastern uplift of Songliao Basin is a half-graben (Fig. 3B), which overlaps towards the northeastern Yangdachengzi Bulge and is limited by the western Sangshutai Fault (Fig. 3C). The burial and geothermal history of the Jurassic-Cretaceous successions was constructed on well SN17 (Fig. 4) in the central depression (Xu et al., 2020a). This reveals rapid burial at 118 Ma and minor uplift at 116 Ma during the K_1sh depositional period. The Shahezi Formation achieved a maximum vitrinite reflectance of 1.4% to 1.5% at the end of the Cretaceous.

3. SAMPLING AND METHODS

3.1. Sampling description

This study analyzed core (1–2 cm thick) from the Cretaceous sequence (K_1sh to K_1qn) sampled at 1 to 2 m from well JLYY1 for geochemical pyrolysis logging and RoqSCAN SEM-EDS (scanning electron microscope and energy-dispersive X-ray spectroscopy) analyses. Large core blocks (4–5 cm thick) from the K_1sh section were further sampled at ~0.4 m spacing for geochemical, mineralogical, and organic petrographical analyses. Shales and mudstones were the focus with care taken to avoid sampling sandstone, siltstone, and carbonate-rich intervals.

3.2. Geochemical pyrolysis-flame ionization detector (FID) logging

The geochemical pyrolysis FID logging was performed on the drilling cuttings at the JLYY1 well site marked in Fig. 3C, following the Chinese Petroleum and Natural Gas Industry Standard (SY/T 5778-2008, Specifications for logging of oil and gas wells by rock pyrolysis). The YQZF-1 Oil & Gas Component Analyser (HaiCheng Petro Chemical Instrument Factory, China) was employed to measure the Rock-Eval parameters (excluding S_3), pyrolyzed carbon (PC) concentrations, and light hydrocarbon gases (S_0 peak). This device is derived from Rock-Eval and is usually called Oil Show Analyzer (Espitalié et al., 1984). A detailed experimental procedure can be found in Wang et al. (2023). The pyrolysis indices generated by this method are listed in Table 2. Notably, unlike Rock-Eval, both peak S_3 and Oxygen Index (OI = S_3/PC×100, mg HC/g C_{org}) data are unavailable from this equipment because the quantity of CO_2 generated from the cracking of kerogen is not determined (Espitalié et al., 1984; Tissot and Welte, 1984; Peters, 1986).

3.3. TOC/TS/TN concentrations and organic carbon isotopes

Bulk rock TOC, total sulfur (TS), and total nitrogen (TN) concentrations were determined on 136 samples. Bulk C and S concentrations were measured by a LECO CS230 C/S Determinator. The total nitrogen (TN) amounts in four bulk samples were measured with an Elementar vario EL cube EA. The absolute precisions are better than ± 0.1 wt % for C/S and ± 0.3 wt % for TN. Sample powders were decarbonated by treatment with 6 *M* hydrochloric acid. The dried, carbonate-free, residue was tested for organic carbon isotopic composition ($\delta^{13}C_{org}$) using a Thermos Fisher Scientific Delta V Plus isotope ratio mass spectrometer with precisions of better than ± 0.1 ‰. The results were calibrated against a global standard (USGS24 Graphite, $\delta^{13}C$ = -16.05 ‰) and Chinese national standard (GBW004408, $\delta^{13}C$ = -36.9 ‰), expressed relative to the Vienna Pee Dee Belemnite (VPDB) international standard.

3.4. RoqSCAN SEM-EDS and FIB-SEM

The RoqSCAN system is a quantitative and fully automated SEM-EDS for mineralogical, geochemical, and petrophysical studies, developed jointly by Fugro Robertson Ltd. and Carl Zeiss Microscopy Ltd (Ashton et al., 2013). Equipped with a Carl Zeiss EVO 50 SEM, a Bruker AXS X-ray detector, a Bruker Pulse Processor and SmartPI™ software, the RoqSCAN provides real-time digital images revealing compositional and textural features of rocks within one hour. In this study, 178 samples were embedded into 30-mm epoxy resin round blocks, and then polished and carbon-coated (Oliver et al., 2013). Next, samples were assessed by RoqSCAN SEM-EDS to determine their mineralogical composition and textural information. Massive versus laminated structure within shales and mudstones could be differentiated via RoqSCAN, further contributing to TOC and mineralogical lithofacies classifications.

SEM photomicrographs and SEM-based mineral maps can provide direct visual evidence of mineral particles, dispersed organic matter (OM), and OM-hosted pores, at the µm to nm scale. Ar-ion beam cross-sectional milling was applied to polish the sample surface before SEM observation. Backscattered (BSE) and secondary electron (SE) microscopy were performed to identify mineral morphology and types using a Zeiss GeminiSEM 450 were conducted at 20 kV accelerating voltage, 1 nA current, and 10 mm working distance. An FEI Helios Nanolab 650 Dual Beam FIB (focused ion beam)-SEM system was employed to image dispersed organic particles and associated micro-scale pores with a beam current of 5 nA, an accelerating voltage of 2.00 kV, and a working distance of 3.5 mm. A Thermo Scientific Apreo 2 SEM system with dual EDS detectors (Bruker XFlash Series 6) was used to image minerals and sedimentary structures of calcite-rich laminae. EDS spectra were collected at 8 ms acquisition times and 200 nm steps and further processed by the Thermo Scientific™ Maps Mineralogy Software to generate high-resolution mineral maps.

3.5. Organic petrography

Whole rock pieces of four core samples were embedded in epoxy resin and mechanically polished along the direction perpendicular to sedimentary bedding. Maceral compositions were analyzed with a Leica DM4500P microscope equipped with a 50× oil immersion objective under reflected white and UV/blue fluorescence light. Five groups of organic particles were differentiated following the petrographic classification scheme proposed by ICCP (1998 and 2001) and Mastalerz et al. (2018): (i) vitrinite; (ii) liptinite; (iii) inertinite; (iv) zooclasts; and (v) secondary products. The same microscope, with a CRAIC 308 PV_{TM} Spectrophotometer, was employed to measure vitrinite reflectance (R_o) under reflected light at 546 nm wavelength (1.518 refractive index oil). Reflectances were calibrated with an yttrium aluminium garnet standard of known reflectance (0.916%). More than 30 measurements were collected on each sample to obtain the minimum, maximum, and standard deviation of R_o.

Correlative light and electron microscopy were employed to identify maceral types, following the SEM petrographic characteristics of macerals summarized in prior studies (Liu et al., 2017; Liu et al., 2019b; Liu et al., 2022a). Eleven ion-milled samples were examined under FIB-SEM, and then the same fields of view were examined under an optical microscopy in reflected white light. Rock fabrics, biological structures, microfractures, and special components (e.g., pyrite framboids and fossils) can be used for rapid positioning.

3.6. X-ray diffraction (XRD) tests, major and trace element analysis

XRD analyses were conducted on five representative samples. Rocks were crushed into silt-size powder with a tungsten disc mill (Retsch RS 200, Germany). For each sample, 5 g of powder was mixed with 12 mL of distilled water and then crushed to powder <10 μm for 10 minutes using a micronizing agate mill (Retsch XRD-Mill McCrone). The resultant slurry was dried at 60°C for 24 hours, crushed into a light and loose powder using an agate mortar and pestle, and back loaded into cavity holders as randomly oriented powders. A PANalytical X'Pert Pro MPD X-ray Diffractometer, equipped with a Copper X-ray tube and a Ni filter, was employed to scan the powders in a 2Theta range of 4–70°2θ. To assess the presence of swelling clay minerals (smectite); samples were saturated with ethylene glycol (EG), by the vapor pressure method, at 60 °C for 15 h and rescanned. HighScore Plus® analysis software attached to the ICDD PDF 4+ database (International Centre for Diffraction Data, Powder Diffraction File 4+ Release 2020) was used to determine the mineral abundances based on the Relative Intensity Ratio (RIR) method (Snyder, 1992).

X-ray fluorescence spectrometry (AL104L, Axios mAX) and inductively coupled plasma mass spectrometry (ICP MS, ELEMENT XR) were respectively used to measure the major and trace element concentrations of core samples. Rock reference materials were analyzed along with samples to monitor the data qualities: the USGS rock reference materials (SDO-1, SCo-1, and SGR-1) for major oxides and the Chinese National standards (GBW07428, GBW07429, and GBW07430) for trace elements. Analytical uncertainties based on replicate analyses are better than ± 5 % (2σ).

4. RESULTS

4.1. Depositional settings and facies interpretations

4.1.1. Fan-delta facies

The Shahezi Formation in the Lishu Rift Depression is dominated by fan-delta deposits, which are located adjacent to faults and rift slopes (Fig. 5). Subaerial fan-delta plain deposits are composed of thickly-bedded conglomerates, gravel-bearing sandstones, sandy mudstones, and interbedded carbonaceous mudstones and coals in places (Figs. 5 and 6B). Massive or normal-graded conglomerates and sandstones with rounded to sub-angular pebbles are interpreted as braided channel fills (e.g., Kleinspehn et al., 1984; Wood and Ethridge, 1988). Fine-grained sandstones interbedded with mudstones and coals are interpreted to be interchannel deposits (e.g., Feng et al., 2013). Fan-delta front subfacies contains relatively thinner and finer-grained deposits than the fan-delta plain; these include gravel-bearing sandstones, fining to medium sandstones, thinly interbedded siltstones, and mudstones. Massive or fining upward conglomeratic sandstones, characterized by round to subrounded granules, erosive bases, and current beddings, are interpreted to be subaqueous channel fills (e.g., Kleinspehn et al., 1984; Wood and Ethridge, 1988; Yang et al., 2020) (Fig. 6C and D). The channel sandstones exhibit gradual or abrupt contact with overlying interchannel mudstones (Fig. 6E), and have sharp, and locally erosional, contacts with underlying mudstones; where core is not available, box-shaped, and bell-shaped wireline log motifs support the interpretation of abrupt contacts (Fig. 6A). The basal erosional surfaces are locally associated with angular and granule- to pebble-sized mud clasts, which are probably reworked rip-ups from the pro-fan deltaic or lacustrine mudstones (Fig. 6C). Mouth bar deposits change upward from mudstones to muddy siltstones with increasing intercalated cross-bedded siltstones and fine sandstones, characterized by parallel, flaser, wavy beddings (Fig. 6F and G) and funnel-shaped wireline log curves (Fig. 6A). Pro-fan deltaic deposits are composed of gray to black mudstones, which are massive or laminated and locally display soft-sediment deformation (ball and pillow structure) when intercalated with mouth bar siltstones (Figs. 7 and 8A).

4.1.2. Lacustrine facies

A 90-meter-thick lacustrine succession, in the middle of Shahezi Formation, is separated into lower shale and upper mudstone sections by a middle gravel-bearing medium sandstone (Figs. 6 and 7). Both the shale and mudstone have complex mineralogy, predominantly composed of clay minerals (65.88% on average) with minor silicate framework grains (23.67% on average) and carbonates (10.44% on average) (Figs. 9E, 9F, 10E, 10F, and 11A). Illite and interstratified illite/smectite (I/S) are the two most abundant clay minerals; the chlorite and kaolinite contents are lower than 15% (Fig. 11A). Both the illite and kaolinite present as interparticle pore filling matrix (Fig. 12A), whereas chlorite occurs as ordered grain coats or inclusions in solid bitumen (Fig. 12B–F). The grain-coating chlorite comprises both bladed crystals perpendicular to the host quartz grains, and aggregates of crystals that are parallel to the bedding. Smectite occurs as mixed layers with illite, indicated by the significant changes in the diffraction patterns (expansion of d_{001} from 6.18° 2θ/14.29 Å to 8.88° 2θ/9.95 Å) caused by EG solvated preparation (Fig. 11B). The non-clay mineral silicate fraction is dominated by quartz (16.8% to 41.4%) with relatively few feldspar grains (0 to 5.7%) (Fig. 11A). As shown in SEM images, quartz occurs as silt- to clay-size detrital particles (Fig. 12E), euhedral crystals (Fig. 12B and F), and overgrowth rims (Fig. 12F). Authigenic quartz overgrowth formed before grain-coating chlorite (Fig. 12F). Carbonates are present as cryptocrystalline laminae (Fig. 8F) and cements (Fig. 10A), microcrystalline particles (Fig. 10A), bedding-parallel fracture-filling sparry calcites (Fig. 10D), parallel aligned shell fragments (Fig. 9A), and sub-mm-scale carbonate bands (Fig. 9A). Pyrite is present in the lower shales as pyrite framboids and discontinuous μm-scale laminae (Fig. 9B and C).

Eight shale/mudstone lithofacies were defined to investigate the lacustrine subfacies and their vertical change, following the nomenclature proposed by prior studies (Lazar et al., 2015; Ma et al., 2016; Figs. 7, 9E, 9F, 10E, and 10F): (1) organic poor (TOC < 1%) and organic rich (TOC > 1%); (2) siliceous (total non-clay mineral silicates > 50%), argillaceous (total clay minerals > 50%), calcareous (total carbonates > 50%), and mixed (no component is greater than 50%); (3) massive and laminated. The lacustrine deposits vary in composition from organic-rich laminated shales to massive mudstones, interbedded with stratified siltstones and tuff layers, which are interpreted as the following subfacies.

4.1.2.1. Lake shore to littoral beach-bar subfacies. The lake shore to littoral beach-bar subfacies is composed of well-sorted and well-rounded siltstone and muddy siltstone layers, which are too thin (<0.2 m) to be recognized from geophysical logs (Fig. 7). A fining-upward siltstone layer in Fig. 8B overlies a flat erosion surface, suggesting that this unit was deposited in a proximal setting and recorded the transition from the shoreline to offshore. The small-scale flaser bedding and soft-sediment deformation (e.g., flame structure) indicates that this subfacies resulted from relatively strong wave conditions in a shallow water setting (Fig. 8B). The hummocky cross stratification, characterized by low angle curved laminae and upper erosional surfaces truncating the hummocks and swales, shows the influence of proximal storm current (Cheel and Leckie, 1993; Fig. 8C).

4.1.2.2. Shallow-littoral mudstone subfacies. The RoqSCAN mineral maps and SEM-EDS images show that the shallow-littoral subfacies is dominated by massive and argillaceous mudstones (Figs. 10A–C). These mudstones are characterized by limited quantities of OC (TOC = 0.05%–0.42%), homogenous fabrics, discontinuous silty laminae (Fig. 8D), and horizontal burrows filled with pyrite nodules (Fig. 8E).

4.1.2.3. Sublittoral subfacies. The black, laminated (mm to sub-mm) and variably calcareous shales were deposited in a sublittoral environment. In comparison to other subfacies, these shales have a higher quantity of carbonate minerals, which are predominantly calcite (4.20%–97.44%) and present as shell laminae (Fig. 9A), sparry bands (Figs. 9A and 10D), and microcrystalline matrix (Fig. 10A). The contributions of dolomite to whole rock sample are typically less than 1.5%. In some cases, the deposits are almost entirely calcified, which occur as thick, continuous, calcite-rich laminae alternating with thin, discontinuous clay mineral-rich laminae (Fig. 8F).

4.1.2.4. Profundal subfacies. The distal and profundal subfacies are finely laminated (sub-mm, Figs. 8I, 9B, and 9C) black shales. The generally continuous and parallel laminae are composed of quartz grains, scattered pyrite, and framboidal pyrite aggregates (Fig. 9B and C). These shales display high organic enrichment (up to 4.63% TOC) and low hydrocarbon generation potential (HI < 110 mg HC/g TOC), which is contributed by the widely dispersed land plant debris as shown in hand specimen and large-area FIB-SEM images (Fig. 8H and J). There is a negligible presence of shallow water bioclastic detritus in this subfacies, which are minor fragments of disarticulated and presumably transported-in bivalves (Fig. 8G).

4.1.3. Sublacustrine fan facies

The sublacustrine fan deposits recovered by JLYY1 occur as a 3.47-meter-thick bed in the middle of lacustrine succession (Fig. 7). These deposits, composed of dark, matrix-supported pebbly mudstones, can be easily recognized on geophysical logging curves due to their low GR and DT intensities in a background of high values (Fig. 6A). As indicated by the RoqSCAN mineral map and the geochemical pyrolysis-FID test, these immature sediments, containing higher contact of angular to sub-angular quartz pebbles and plagioclase particles than lacustrine mudstones, is characterized by high TOC (2.38%) and low HI values (13.97 mg HC/g TOC) (Fig. 6H and I). Subaqueous gravity-flow sediments in deep lacustrine environments, known as sublacustrine fans, are typically associated with fault-controlled sediment supply from adjacent fan delta systems (Soreghan et al., 1999; Nelson et al., 1999). The sublacustrine fan and its sediment supply might be controlled by the adjacent intra-depressional faults and fan delta deposits (Fig. 5).

4.1.4. Volcaniclastic facies

Volcanogenic tuffs occur as thin, greyish green, and yellow layers (<2 cm thick) in sublittoral and profundal shales throughout the lower part of lacustrine succession (Figs. 7, 8K, and 8L). These fine-grained deposits result from airborne volcanic ash deposited into low-energy lake environments. XRD results reveal that they are predominantly composed of illite/smectite minerals, with minor quartz and chlorite (Fig. 11). EG solvation produced two weak but clearly identified reflections (7.15° 2θ/12.34 Å and 9.41° 2θ/9.39 Å), indicating an ordered structure of R1 illite(0.7)/smectite (Fig. 11C). The 7.55° $\Delta 2\theta$ determined by the other two peak positions (9.41° and 16.96° 2θ) also confirm this diagnosis (Moore and Reynolds, 1989).

4.2. Stratigraphic sequence

The sequence stratigraphic architecture of nonmarine successions is recognized by vertical changes of stratal units (e.g., depositional facies and multi-scale sequences) and identification of sequence boundaries (e.g., unconformities and their correlative conformities, flooding surfaces, and changes in stacking patterns); this approach has been adapted and modified from the study of marine sequence stratigraphy (Shanley and McCabe, 1994; Lin et al., 2001; Catuneanu et al., 2009; Catuneanu et al., 2011; Catuneanu, 2022). Nonmarine depositional sequences can be subdivided into systems tracts (e.g., lowstand, transgressive, and highstand systems tracts), following a symmetrical cycle of variation in the ratio of accommodation to sediment supply (A/S) through time (e.g., Shanley and McCabe, 1994; Pietras and Carroll, 2006, Lin et al., 2001; Feng et al., 2013). However, as the deltaic-lacustrine Shahezi Formation was deposited during the most intense rifting phase of the Songliao Basin (Wang et al., 2016; Wang et al., 2021), it shows typical characteristic of rift sequences, e.g., short retrogradational portions, long stages of progradation, absent to poorly developed lowstand systems tracts, and the strong asymmetry of base-level curves (Figs. 5 and 6; Martins-Neto and Catuneanu, 2010). Here, following the sequence stratigraphical interpretation of Shahezi Formation in prior studies (Jia et al., 2016; Cai et al., 2017; Wang et al., 2017b; Deng et al., 2021), we used sequence stratigraphical principles developed for the nonmarine deposits and rift successions to interpret the inland deltaic-lacustrine depositions of Shahezi Formation. In addition, based on the lake models established in prior studies (Bohacs, 1998; Bohacs et al., 2002; Pietras and Carroll, 2006, Bohacs et al., 2007; Passey et al., 2010), the fine-grained lacustrine sediments of Shahezi Formation are further subdivided into four subfacies and a few cyclic, parasequence-order packages (see Sections 4.1.2 and 4.2.3; Fig. 7) to understand the high-resolution lake sequences and OC burial process.

4.2.1. Sequence boundaries

Sequence boundaries, typically marked by changes in stratal stacking patterns and basinward shifts in facies, are highly variable in continental lake basins (Bohacs et al., 2007). Their depositional expression critically depends on paleogeography, accommodation, sedimentation rates, and proximity to sediment sources (e.g., Picarelli and Abreu, 2012). To investigate the lateral relationships between time-equivalent deposits and understand the paleogeographic location of depositional site within the rift depression, three second-order sequence boundaries (T5, T42, and T41) have been identified and correlated through four wells from basin center to margin (Fig. 5). The T5 surface is defined by an angular unconformity between the pre-Triassic volcanic and metamorphic rocks to Upper Jurassic (J_3h) clastic depositions. The Shahezi Formation recovered by JLYY1 borehole was deposited along the southeastern rift slope, bounded by T42 and T41 surfaces. The angular T42 unconformity lies on the top of J_3h Formation, displaying a sharp contact between Huashiling and Shahezi Formations (Fig. 5). T41 displays a transition upward from channel sandstones to pro-delta mudstones, corresponding to gradual changes of logging curves and onlap features on the seismic profile (Figs. 5 and 6). Within the Shahezi Formation, third-order sequence boundaries are represented by channel lag deposits that consist of mud clasts overlying a sharp erosive surface (e.g., the SB2 at 3077.85 m, Figs. 6A, 6C and 7). The SB1 at 3122.05 m displays an abrupt transition upward from shallow-littoral mudstones to pebbly mudstones in sublacustrine fan, characterized by sharp changes of both gamma ray (GR) and resistivity (LLD) log responses (Figs. 6A and 7).

4.2.2. Maximum flooding surface (MFS)

Within nonmarine strata, the maximum flooding surface marks a rapid rise of stratigraphic base level and separate progradational deposition from underlying retrogradational packages (Posamentier et al., 1988; Posamentier and Vail, 1988; Lawrence et al., 1990; Shanley and McCabe, 1994; Catuneanu et al., 2009). In the Shahezi Formation, the MFS is represented by the finely laminated lacustrine shales of distal and profundal subfacies, corresponding to high TOC, GR, acoustic (DT), and low LLD log values (Figs. 5 and 6). It is located at 3140.90 m and separates the overlying shallow-littoral and sublittoral mudstones from the underlying profundal shales (Fig. 7). The lacustrine deposits exhibit a coarsening-upward profile above the MFS, where proximal shallow-littoral mudstones and lake shore siltstones gradually replace the distal profundal-sublittoral shales with time (Fig. 7).

4.2.3. Sequence stratigraphic framework

Based on the interpretation of sequence boundaries, maximum flooding surfaces, and depositional facies, the Shahezi Formation, in the JLYY1 borehole, is defined as a third-order sequence which can be divided into transgressive systems tract (TST) and highstand systems tract (HST) (Fig. 5). The TST is overlain by a maximum flooding surface, represented by fining-upward shifts from fan delta sandstones to lacustrine shales (Fig. 6). The deposits exhibit a coarsening-upward profile in HST, where proximal fan-deltaic conglomeratic sandstones replace the littoral-profundal mudstones (Fig. 6).

A detailed characterization of parasequence-order packages is conducted on the lacustrine-dominated interval within the Shahezi Formation. A parasequence commences in a flooding surface at the bottom of laminated sublittoral-profundal shales and ends at the top of shallow-littoral mudstones, representing one episode of shoreline progradation (Fig. 7). The grain size and bed thickness of shallow-littoral mudstones increase upward from the TST to the HST due to shoreline progradation and water-depth shallowing. At the top of the HST, the parasequence ends at lake shore siltstone beds, which has an erosive base and a fining-upward trend (Figs. 7 and 8B). Based on the interpretation of flooding surfaces and sequence boundaries, the lacustrine-dominated interval can be further divided into four systems tracts (TST-1, HST-1, HST-2, and HST-3).

4.3. Organic carbon: concentrations, types, and thermal maturity

The vitrinite reflectance (R_o), TOC, and HI values of source rocks from the JLYY1 borehole have been compiled in Fig. 13 to investigate the effects of thermal maturation on organic geochemical indices within Shahezi Formation. Most lacustrine shale/mudstones samples are highly mature, confirmed by both vitrinite reflection ($R_o > 1.1\%$) and T_{max} values ($T_{max} > 440$ ℃) (Figs. 13 and 14). TOC and HI values may have been influenced by thermal maturation in the lower part of lacustrine deposits (>3138.4 m) (Fig. 13), with transformation ratios (Table 2; Tissot and Welte, 1984) averaging 0.41 and reaching as high as 0.67. Hence, this section may originally have been richer in organic carbon than that indicated by present-day measurements due to the thermal maturation and hydrocarbon expulsion. In contrast, the measured values of organic geochemical indices from samples shallower than 3117.05 m are regarded as the signals of primary organic carbon burial, as the TOC and HI values increase with burial depth and the corresponding transformation ratios are lower than 0.26 and average 0.10.

The organic fractions of lacustrine mudstones from the Shahezi Formation are predominantly composed of vitrinite (88% to 93%), with minor inertinite (5% to 10%) and secondary solid bitumen (1% to 5%). Correlative reflected light and electron microscopy shows that the silt-size vitrinite and inertinite (terrestrial input) occurred in dispersed particles or elongated bands, and do not develop secondary organic pores (Figs. 15A–F). The highly reflective inertinite particles can be fragmented (Fig. 15B and F) or well-preserved (Fig. 15G) with visible cellular structures derived from land plant detritus. As a secondary product, solid bitumen is characterized by void-filling and embayment textures against minerals, which is different from other primary macerals with specific shapes (Mastalerz et al., 2018; Liu et al., 2022a). Within the Shahezi Formation shales, the amorphous solid bitumen is generally associated with euhedral chlorite blades and quartz microcrystals and hosts secondary nanopores formed by thermal degradation (Figs. 12B–F, 15D, and 15I). Zooclasts can be identified based on their distinct biological structure, e.g., bivalve shell fragments and organic linings of microforaminifera (Fig. 15H).

The lacustrine shales and mudstones of Shahezi Formation have an average TOC of 1.13%, with an upward increase trend in TST-1 and a general decrease trend from HST-1 to HST-3 (Figs. 14 and 16). HI values shows a systematic stratigraphic variation from TST-1 to HST-3. Most of the HI values are lower than 200 mg HC/g TOC. The organic $\delta^{13}C$ values of lacustrine shales/mudstones range from -28.60‰ to -23.10‰ (Fig. 14), which display systematic stratigraphic variation. Nearly all the mudstone samples from HST-2 and HST-3 fall within a relatively narrow range of -23.30‰ to -23.10‰, except for one sample from HST-2 with a $\delta^{13}C_{org}$ of -28.60‰, an HI of 40.82 mg HC/g TOC which may have a greater fraction of land-plant detritus. The TST-1 and HST-1 samples have a relatively lighter organic carbon isotopic composition (-28.60‰ to -24.30‰). Molar TOC/TN ratios of four samples from four systems tracts were used to help reveal the OC sources, which display a decreasing trend from TST-1 to HST-3 (Fig. 14D).

5. DISCUSSION

5.1. Enhanced chemical weathering and warm-humid paleoclimate

As multiple factors, including protolith composition, sediment recycling, post-depositional diagenesis, and carbonate abundance may have potential effects on CIA values, the use of CIA as a proxy, linking chemical weathering with paleoclimate, must be used with caution (Nesbitt and Young, 1982; McLennan, 1993; Cox et al., 1995; Fedo et al., 1995; Panahi and Young, 1997; Panahi et al., 2000). The A-CN-K ternary diagram of molecular proportions of Al_2O_3, CaO^*+Na_2O, and K_2O is helpful for distinguishing weathering-induced compositional variation from sediment provenance (Nesbitt and Young, 1984; Fedo et al., 1995; Panahi and Young, 1997). The initial composition of unweathered rocks (squares on the CN-K sideline in Fig. 17) indicated that rocks in the four systems tracts have similar provenance composition.

Potassium metasomatism results in the conversion of kaolinite to illite when K^+-bearing pore waters are available, which is quite common in shale strata and can decrease CIA values (Fedo et al., 1995). To correct the potassium addition, the CIA values were recalculated (CIA_{corr}) based on the "prealteration" K_2O values (Panahi et al., 2000) (Table 2, Figs. 17 and 18). Additionally, the calculation of CaO* in the CIA_{corr} formula makes a correction for the presence of Ca in carbonates and phosphates (McLennan, 1993). As a result, the CIA_{corr} may be of limited use for carbonate-rich rocks, e.g., the calcareous/mixed shale facies in HST-1. Hence, the $Ln(Al_2O_3/Na_2O)$ index was proposed to provide supplementary evidence (von Eynatten et al., 2003) (Fig. 18). The strong positive correlation between $Ln(Al_2O_3/Na_2O)$ and CIA_{corr} occurs in the HST-1 ($R^2 = 0.73$, p-value < 0.001), indicating that the carbonates has no significant effects on the stratigraphic variation of CIA_{corr} values.

After experiencing multiple events of sedimentation and weathering, recycled rocks tend to have higher CIA values, which may lead to overestimation of chemical weathering intensity. The Index of Compositional Variability (ICV, Table 2, Cox et al., 1995) was used here to estimate the rock compositional maturity and sediment recycling effects. The ICV values of mudstones from HST-2 and HST-3 (0.89 to 2.35, 1.38 on average) are higher than the range of values for feldspars (0.54 to 0.87) and clay minerals (0.03 to 0.78) (Fig. 18), indicating that the upper mudstones are dominated by non-clay mineral silicates and are compositionally immature (Cox et al., 1995). In comparison, the TST-1 and HST-1 with relatively lower ICV values (0.79 to 1.27 with an average of 0.96) may have been subjected to greater influence of sediment recycling than the upper mudstones, which might partly account for their higher CIA_{corr} values. However, as the correlations between ICV and CIA_{corr} are relatively weak ($R^2 = 0.47$, p-value < 0.01 for TST-1, $R^2 = 0.32$, p-value < 0.01 for HST-1), it is suggested that the sediment recycling is not the dominant factor affecting the CIA_{corr} values.

The chemical index of weathering is sensitive to climate change. During the chemical weathering process, the Ca, Na, and K are largely removed from feldspars with decreasing CIA (Panahi and Young, 1997). The chemical weathering rates increase as humidity and temperature increase (White and Blum, 1995) because weathering intensity is determined primarily by the amounts of humic and associated acids percolating into the weathering profile driven by rainfall (Singer, 1980; Nesbitt and Young, 1982; Nesbitt and Young, 1984; Nesbitt and Young, 1989). According to the correlation among CIA values, paleoclimate conditions, and chemical weathering intensities proposed in Fedo et al. (1995), the high CIA_{corr} values of TST-1 and HST-1 indicate a hot and humid climate during the depositional period of the lower shales (Fig. 18). The HST-2 and HST-3, characterized by lower CIA_{corr} values, were deposited in a warm and humid climate with intermittent hot-humid climate fluctuations. The sharp decrease of CIA_{corr} from HST-1 to HST-2, and the gradual decrease of CIA_{corr} in the end of HST-3, represent two cooling and arid events in the lacustrine sequences. Overall, during the Shahezi Formation, the climatic condition was warm-humid in the lake zones. Yan et al. (2017) suggested that the climate during deposition of the Shahezi Formation was mid-subtropical based on algae, palynomorphs, and ostracoda collected from the Lishu Rift Depression. A similar climate condition has also been reported in the rift Fuxin Basin in NE Asia, where the intensive chemical weathering and warm humid climates prevailed during the Early Albian Shahai–Fuxin Formation (Xu et al., 2020b).

5.2. Organic carbon: origins and concentrations

5.2.1. Organic petrographic indicators

The organic fraction of black shales and mudstones can be petrographically classified into several maceral groups, which can be correlated to kerogen types derived from Rock-Eval pyrolysis: liptinite (kerogen type I and II), vitrinite (kerogen type III), inertinite (kerogen type IV), zooclasts, and secondary products (Peters, 1986; Mastalerz et al., 2018; Liu et al., 2022a). For the highly mature Shahezi Formation, macerals are predominantly composed of vitrinite, with minor inertinite and solid secondary bitumen (Fig. 15; Section 4.3), which is consistent with prior studies (Gao et al., 2018; Xu et al., 2022), and can also be supported by evidence from palynological assemblages (43% herbage and 31.6% coniferous plants) (Yan et al., 2017). The absence of liptinites in the Shahezi Formation shales might be caused by the depositional organic assemblage and post-depositional kerogen transformation. With increasing thermal maturation, the primary macerals (e.g., bituminite and alginite) are transformed into secondary products (e.g., hydrocarbon and solid bitumen), and the decrease in liptinitic maceral content is generally accompanied by an increase in solid bitumen content (Liu et al., 2019a).

The original organic assemblages of solid bitumen-rich highly mature shales are mainly contributed by oil-prone macerals during their immature stage (Liu et al., 2022a). For example, in the Upper Devonian Duvernay Formation shales from the Western Canada Sedimentary Basin, the content of bituminites in immature cores (0 to >80%) decreases to <45% in gas-mature cores, whereas the proportion of solid bitumen increases from 5%–55% of immature samples to 65%–100% of gas window sample (Harris et al., 2018). For the Upper Devonian New Albany shale in the Illinois Basin, the bituminite, dominant maceral in the early mature samples, is gradually replaced by solid bitumen from R_o 0.55% to R_o 0.79% (Liu et al., 2019a). Bituminite could not be found in the New Albany shale after the maturity of R_o exceeding 0.8% (Liu et al., 2019a). Similarly, alginite could not be found in the New Albany shale after the maturity of R_o exceeded 1.42% (Liu et al., 2017). Hence, it is suggested that these oil-prone macerals are generally not present after the peak oil window (R_o 0.8%–1.0%) (Hackley and Cardott, 2016; Mastalerz et al., 2018; Liu et al., 2019a, 2022a; Sanei, 2020).

In contrast to oil-prone macerals, the zooclasts and terrestrial-derived macerals (vitrinite and inertinite) with low hydrocarbon generation potential, do not change significantly during thermal maturation and can exist at any stage of thermal maturation (Liu et al., 2017, 2022a). If the organic components of immature source rocks are predominantly contributed by terrestrial input, they will remain enriched in vitrinites and inertinites throughout the whole thermal maturation (Liu et al., 2022a). For example, both the low and high maturity source rocks (R_o 0.5%–1.21%) from lacustrine Karrom Formation, Nyasa Rift Basin (East Africa) are characterized by high abundance of terrestrial-derived macerals (75%–100%) and limited quantities of liptinites (<25%) (Kagya et al., 1991). A similar case can also be found in the shallow marine Snadd Formation from the Nordkapp Basin and Bjørnøya East area (SW Barents Sea), the organic components of which are dominated by Type III/IV kerogens from immature to gas window stages (Abay et al., 2018). For the highly mature Shahezi Formation shales, the original composition of macerals cannot be directly determined due to the lack of immature samples across the entire basin. It is suggested that the Shahezi Formation was mainly contributed by terrestrially-derived OM based on the organic petrographical features of present thermally matured samples, which can be further cross checked by pyrolysis indices, TOC/TN and $\delta^{13}C_{org}$ data.

5.2.2. Pyrolysis indices, TOC/TN, and $\delta^{13}C_{org}$

Pyrolysis experiment and its derived indices (HI and OI) could be used to interpret the origins of OM within black shales, even though they might be affected by thermal maturation and microbial degradation (e.g., Algeo et al., 2004; Harris et al., 2004; Meyers et al., 2006). The high HI values and low OI values indicate a high proportion of lipid-rich type I kerogen derived from algal bodies, whereas the low HI values and high OI values suggest the terrestrial origin of OM (Type III and IV kerogens) (Espitalie et al., 1977). Based on this, the HI vs. OI diagram, HI-T_{max} diagram, and TOC vs. S_2 diagram were proposed to assess the OM sources (Espitalié et al., 1984; Peters, 1986; Langford and Blanc-Valleron, 1990; van Koeverden et al., 2011). In this study, the shales from TST-1 and HST-1, as well as the mudstones from HST-3 have extremely low HI values (Figs. 14, 16, and 19). The low HI values may result from thermal maturation and oxidation of OM, which would have a much greater influence on the labile algal-sourced OM than the refractory type III kerogen (e.g., Katz, 1995; Hasegawa, 1997; Sobek et al., 2009). However, the HI values of HST-2 are anomalously higher than those of the other three systems tracts, and the HI values of HST-1 are lower than those of underlying TST-1, implying that the thermal maturation cannot fully explain the stratigraphic variation of HI. Thus, a very high fraction of terrestrial-derived organic materials delivered to the bottom of rift lake indeed contribute to the low HI values of the Shahezi Formation shales and mudstones.

The variation of TOC vs. HI correlation in HI/OI plots can be regarded as a potential indicator for the variation of OM sources, considering the effects of OC oxidation and thermal maturation (Fig. 20D and E). The fluctuations of HI closely follow TOC concentrations; they are positively correlated where organic enrichment is enhanced by good preservation of Type I kerogen (oil-prone algal material with high inherent HI) and they are inversely correlated where increasing TOC is contributed by increased concentration of type II/III kerogen (gas-prone woody and coaly OM with low inherent HI) (e.g., Beckmann et al., 2005; Passey et al., 2010). Significant positive correlations between TOC and HI have been reported for the Lower Cretaceous lacustrine mudstones, e.g., Upper Aptian–Lower Albian Codo Formation shales in the São Luís graben basin ($R = 0.778$, $p\text{-value} < 0.001$) (Bastos et al., 2020), Aptian Marnes Noires–Argilles Vertes Formation in Congo rift basin ($R = 0.595$, $p\text{-value} < 0.01$) (Harris, 2000; Harris et al., 2004). These correlations indicate that OM accumulation and preservation are dominated by oil-prone macerals of aquatic origin (Dean et al., 1986). In comparison, there is no correlation between TOC and HI in the mudstones of Lower Cretaceous Shahezi Formation ($R = -0.418$, $p\text{-value} > 0.05$) recovered from JLYY1 borehole, which can also be supported by the Rock-Eval data of Shahezi Formation shales from the ICDP SK-2 borehole ($R = -0.072$, $p\text{-value} > 0.1$, Fig. 20D). If the terrestrial OM only accounts for a small proportion of the total organic fraction, the shales are characterized by a strong positive correlation between TOC and HI (e.g., Algeo et al., 2004). Thus, the organic fraction of the Shahezi Formation is predominantly contributed by terrestrially-sourced OM, which is apparently different to other Lower Cretaceous sediments mentioned above. The low HI values have been affected by thermal maturation but are determined primarily by the OM origin.

The photosynthetic land plants preferentially absorb lighter carbon ($\delta^{13}C$ = -7‰) from atmospheric CO_2 than the inorganic carbon in dissolved bicarbonate ($\delta^{13}C$ = 0‰) used by aquatic algae, resulting in relatively ^{13}C-depleted terrestrial OM (Meyers, 1994; Hasegawa, 1997; Hoefs, 2009). In addition, according to the investigation of modern lake sediments, aquatic algae, rich in amino acids and carbohydrates, have lower TOC/TN values ($4 < TOC/TN < 10$) than vascular land plants dominated by lignin and cellulose ($TOC/TN \geq 20$) (Meyers, 1994; Ogrinc et al., 2005). Thus, rocks containing mostly terrestrial OM have lighter (more negative) $\delta^{13}C_{org}$ values and greater TOC/TN ratios than rocks dominated by aquatic OM (Arthur et al., 1985). For the Shahezi Formation mudstones, the organic carbon isotopic composition of the Shahezi (-28.60‰ to -23.10‰) is lighter than that of modern marine OM (-22‰ to -18‰) (Emerson and Hedges, 1988; Meyers, 1994) and is close to that of modern terrestrial OM (-23.0‰ to -33.0‰) (Dean et al., 1986; Meyers, 1994) (Fig. 14D). In addition, the TST-1 and

HST-1 samples have a relatively lighter $\delta^{13}C_{org}$ (-28.60‰ to -24.30‰) and greater TOC/TN ratios than the HST-2 and HST-3 samples (Fig. 14D), indicative of more abundant terrestrial-derived OM within the lower organic-rich black shales than the upper mudstones.

5.3. Stratigraphic variation of organic carbon sources and concentrations

The OC source and concentration display a good response to sequence stratigraphic evolution, indicated by the systematic stratigraphic variation of TOC and HI from TST-1 to HST-3 (Figs. 16 and 19). TOC increased in TST-1 with increasing base-level from lake shore to littoral beach bar to profundal subfacies. The most organic-rich beds occur just above the MFS at the base of HST-1. The relatively low TOC values at the MFS may reflect a combination of slightly low terrestrial OM delivery and high dilution by hydrogen-poor biogenic material (e.g., shell fragments in Fig. 8G, and 16.4% of total carbonates in Fig. 16). From HST-1 to HST-2, TOC reaches its second peak before the sublacustrine fan deposition and then decreases to 0.05% at the end of HST-2 (Figs. 16 and 19). In this period, the HI values show a generally increasing trend, which is interpreted to result from decreased terrestrial OM input and enhanced preservation of aquatic OM during the slow regression period. The matrix-supported pebbly mudstones in the sublacustrine fan is characterized by highly varied TOC values that average in 1.12% and range between 0.17% and 2.38%. An abrupt decrease of HI values occurs at the transition from HST-2 to HST-3 (Fig. 16), corresponding to a high-order flooding surface revealed by RoqSCAN images (Fig. 10C).

As the base-level increased towards the MFS within TST-1, the OM types became more terrigenous (Type III/IV kerogen), and thus increasingly gas-prone, also reflected by the decreasing HI values (Figs. 16 and 19). TOC generally decreased when the base-level decrease in HST-1, whereas HI gradually increase in this interval (Fig. 16). The fraction of aquatic-sourced OM (Type I oil-prone kerogen) in the shallow-littoral mudstones of HST-2 with peak HI values is higher than that in the sublittoral-profundal shales of TST-1 and HST-1 (Figs. 14 and 16). The stratigraphic changes of TOC and HI presented here are not consistent with OC enrichment pattern in Early Cretaceous marine shale dominated by aquatic OC (Bohacs et al., 2005; French et al., 2022). In other words, in contrast to marine sediments controlled by aquatic productivity, organic carbon accumulation in the syn-rift lake during the Shahezi Formation, dominated by terrigenous OC input, cannot be simply explained by the interaction between organic production, destruction, and dilution.

The lacustrine mudstones of the Shahezi Formation were deposited in an over-filled lake basin where the parasequence development is driven predominantly by fan-deltaic channel avulsion and shoreline progradation (Figs. 5 and 6; Carroll and Bohacs, 1999; Bohacs et al., 2000). Abundant input of land-derived OM dominates the variability in OM types and concentrations of the Shahezi Formation (e.g., Bohacs, 1998). The land-plant material produced in lake plain can be transported into the lake water column and then deposited in littoral-profundal sediments. The mm-scale phytoclasts and rounded to subrounded µm-scale OM particles that are widely dispersed within the finely laminated profundal shales support this interpretation (Fig. 8G–J). The transportation of terrestrial OC into the lake basin may have been enhanced by the relatively steep slope that was created during the development of the syn-rift basin; this control has been demonstrated by sedimentological data and geochemical modelling results from prior studies (Harris et al., 2004; Harris and Tucker, 2015). For the Shahezi Formation, the wide development of fan deltas (Fig. 5) suggests the high-gradient slope produced in the maximum rifting phase (e.g., Sohn, 2000). In addition, the unstable lakebed triggered by the intra-depressional faults may also have transferred the OC-bearing sediments into lake basin, e.g., the pebbly mudstones in the sublacustrine fan subfacies (TOC = 2.38%, HI = 13.97 mg HC/g TOC, Figs. 5 and 6). The lithological shift from lower shales to upper mudstones witnessed a decreased base-level, which would have led to a loss of peat swamps and a low input of land plant detritus. The lithological shift also explains why the TOC concentration in HST-3 remains at a low level (<1%) with low HI values (Figs. 16 and 19).

5.4. Climate controls on the organic carbon sources and concentrations

The paleoclimate change (Figs. 18 and 19) may also have contributed to the change in the OC type and concentration. The warm and humid climate during the Shahezi Formation promoted the terrestrial OC production, accelerated the hydrologic cycle in the rift lake catchment, and led to enhanced chemical weathering (Nesbitt and Young, 1984; Nesbitt and Young, 1989); this was associated with increased continental runoff, and greater terrestrial OC input from continents into the lake (Hall and Smol, 1993; Harris et al., 2004; Meyers et al., 2006; Harris and Tucker, 2015). In addition, the high chemical weathering rates can introduce mineral-derived nutrients into lakes, as indicated by the positive correlation between CIA_{corr} and P/Ti ($R^2 = 0.45$, p-value < 0.001) (Fig. 18). From HST-1 to HST-3, the gradual change of climate from warm-humid to cold-arid, suggested by decreasing CIA_{corr}, was accompanied by the decreased lake base-level (Fig.19). The weakened hydrological cycle and reduced production of land plants would have resulted in the decreased terrestrial OC input, as suggested by the positive correlation between CIA_{corr} and TOC (Fig. 20B).

5.5. Organic carbon burial from syn-rift to post-rift lake basin: correlating high- and low-paleolatitude sedimentary records

The Aptian Sialivakou–Djeno Formations from the Congo Basin, western Africa (Harris et al., 2004), represents a potential comparison to the Middle Aptian-Lower Albian Shahezi Formation in the Songliao Basin (Fig. 20). Both the Shahezi shales (118 to 111 Ma) and the Sialivakou–Djeno shales (125 to 117 Ma) were deposited during the active rift phase of lacustrine basins and have similar TOC concentrations (Shahezi: 0.05% to 4.63%, 1.51% on average; Sialivakou–Djeno: 1.1% to 3.28%, 2.16% on average). However, the organic petrologic identification and a positive correlation between TOC vs. HI ($R = 0.709$, $p\text{-value} < 0.05$, Fig. 20E) suggests that total organic carbon burial in the Sialivakou–Djeno shales was largely contributed by aquatic-sourced OM. It is worth considering why the two coeval shale sequences differ in organic carbon type. In addition, the two lacustrine basins, formed at the same time, may have different mechanisms controlling OM accumulation.

The Sialivakou–Djeno shales in the Congo Basin were deposited in an equatorial to near-equatorial region, which was characterized by evaporite development and arid paleoclimate (CIA_{corr}: 53.56 to 66.23, 60.61 on average) (Fig. 20A and C) (Boucot et al., 2013; Scotese, 2016; Cao et al., 2017). The high TOC values of the Sialivakou–Djeno shales do not correspond to the peak values of CIA_{corr}, implying that enhanced continental weathering did not trigger a great input of terrigenous OC. In comparison, the Shahezi Formation in the Songliao Basin was in the boreotropical region characterized by a warm and humid climate (Fig. 20A) (CIA_{corr}: 75.78 to 91.31, 86.51 on average). The more abundant herbaceous and coniferous plants during Shahezi Formation were available to deliver a larger fraction of weathering-influenced terrestrial OM to the lake than the time-equivalent Sialivakou–Djeno shales in Congo Basin.

The origin of OM within all the Cretaceous lacustrine shales from high- and low-paleolatitudes shows a good response to the rift sequence evolution (Fig. 20; Harris, 2000; Harris et al., 2004; Tong et al., 2018). Harris et al. (2004) suggested that the portion of aquatic OC and the importance of aquatic production increased from the active (Sialivakou–Djeno Formations) to the post-rift phase (Marnes Noires–Argilles Vertes Formations), which is marked by a transition of $\delta^{13}C_{org}$ vs. TOC correlation. A similar pattern may also be present in the Cretaceous lacustrine successions of the Songliao Basin. From the active rift phase (Shahezi Formation) to post-rift phase (Nenjiang Formation), the OM tends to be more aquatic-derived (Type I oil-prone kerogen) as the amount of OM increases (Fig. 20D–E). As the tectonic lakes change from active to post rift stages, they become more productive with the slope gradient decreased. In this process, the roles of aquatic productivity and the contribution of algal remains become more important in the burial of lacustrine OC, as suggested by the increased and correlated TOC and HI (Fig. 20D and E). In the post-rift Songliao lake (Nenjiang and Qingshankou Formations), the terrestrial OC input gradually become limited in nearshore facies (Katz, 1995; Petersen et al., 2010), rather than the distal and profundal facies reported in this study. Thus, the tectonic process of rift lake basins may control the sources and concentrations of OC in lacustrine sediments on a large scale, which is responsible for the long-term organic carbon burial in hinterland environments.

6. CONCLUSIONS

(1) The Early Cretaceous (Middle Aptian–Early Albian) Shahezi Formation recovered from well JLYY1 from the Lishu Rift Depression, Songliao Basin, NE Asia is dominated by fan-deltaic and lacustrine facies with a sublacustrine fan bed and volcanic tuff layers developed in the lacustrine mudstone interval. The sequence stratigraphic architecture of the Shahezi Formation has been established on the basis of integrated sedimentological and petrological methods. Fine-grained lacustrine sediments have been subdivided into four subfacies (lake shore to littoral beach-bar, shallow-littoral mudstone, sublittoral, and profundal) and a few parasequence-order packages to establish the high-resolution sequences.

(2) The high OC concentration of the highly mature mudstones and shales from the Shahezi Formation lacustrine sequences was predominantly contributed by terrestrial-derived OC (gas-prone Type III/IV kerogen), suggested by multiple independent proxies (identification of macerals under the correlative light and electron microscopy; pyrolysis indices, TOC/TN, and $\delta^{13}C_{org}$). The OC source and concentration display a good response to sequence stratigraphic evolution and paleoclimate change, indicated by the systematic stratigraphic variation of TOC, HI, and CIA indices. The high enrichment of terrestrial OC in the profundal laminated shales may be resulted from a combination of the steep syn-rift slope, the warm-humid climate, abundant vegetation, and the subaqueous transport of OC-bearing sediments (i.e., matrix-supported pebbly mudstones). The organic carbon accumulation in the Shahezi Formation cannot be simply explained by the interaction between organic production, destruction, and dilution. The validity of using the bioproductivity-based models to explain the organic enrichment within the syn-rift lacustrine sediments dominated by terrigenous OC input needs to be questioned because of the different sources of OC and their controls.

(3) Comparison of two time-equivalent terrestrial records from high (Shahezi Formation, Songliao Basin) and low paleolatitudes (Sialivakou–Argilles Vertes Formation, Congo Basin) suggests that the shift from an active rift phase to a post-rift phase was accompanied by an increase in TOC concentration and a change towards Type I kerogen of aquatic origin. The tectonic processes that influence rift lake basins may control the changes in lacustrine OC sources and concentrations, which are responsible for the long-term OC burial in hinterland environments.

ACKNOWLEDGEMENTS

We would like to thank Jianfang Hu and Shuangbiao Han for providing the Rock-Eval data of Santonian Nenjiang Formation shales (YWC section, Songliao Basin) and Aptian–Albian Shahezi Formation shales (ICDP SK-2 borehole, Songliao Basin). Discussions with Longyi Shao, Xiaotao Xu, Ming Yuan, and Leibo Bian improved the research quality. Two anonymous reviewers are thanked for their constructive comments. The Scanning Electron Microscopy Shared Research Facility (SEM-SRF) at the University of Liverpool is highly appreciated for supporting this research and providing ultra-high-resolution SEM-EDS equipment.

FUNDING

This study was financially supported by State Key Laboratory of Petroleum Resources and Prospecting, China University of Petroleum (Grant No. PRP/open-2217), State Key Laboratory of Shale Oil and Gas Enrichment Mechanisms and Effective Development (Grant No. 33550000-22-ZC0613-0268), China Geological Survey (Grant No. DD20190115), the National Science and Technology Major Project of China (Grant No. 2017ZX05009001), the University of Liverpool and China Scholarship Council Awards (Grant No. 202009110097), and the 2021 AAPG Foundation Grants-in-Aid award.

APPENDIX A. SUPPLEMENTARY MATERIAL

DATA AVAILABILITY

Datasets related to this article are provided in the online supplementary material and can be also downloaded at http://dx.doi.org/10.17632/fgn2chjdnz.1.

REFERENCES CITED

Abay, T.B., Karlsen, D.A., Pedersen, J.H., Olaussen, S., Backer-Owe, K., 2018. Thermal maturity, hydrocarbon potential and kerogen type of some Triassic-Lower Cretaceous sediments from the SW Barents Sea and Svalbard. Petroleum Geoscience 24, 349-373.

Algeo, T.J., Schwark, L., Hower, J.C., 2004. High-resolution geochemistry and sequence stratigraphy of the Hushpuckney Shale (Swope Formation, eastern Kansas): implications for climato-environmental dynamics of the Late Pennsylvanian Midcontinent Seaway. Chemical Geology 206, 259-288.

Arthur, M.A., Dean, W.E., Claypool, G.E., 1985. Anomalous 13C enrichment in modern marine organic carbon. Nature 315, 216-218.

Arthur, M.A., Sageman, B.B., 1994. MARINE BLACK SHALES: Depositional Mechanisms and Environments of Ancient Deposits. Annual Review of Earth and Planetary Sciences 22, 499-551.

Ashton, T., Ly, C.V., Spence, G., Oliver, G., Portable Technology Puts Real-time Automated Mineralogy on the Well Site. In, SPE Unconventional Resources Conference and Exhibition-Asia Pacific. 2013, SPE-166982-MS.

Bastos, L.P.H., Pereira, E., da Costa Cavalcante, D., Ferreira Alferes, C.L., Jorge de Menezes, C., Rodrigues, R., 2020. Expression of Early Cretaceous global anoxic events in Northeastern Brazilian basins. Cretaceous Research 110, 104390.

Beckmann, B., Wagner, T., Hofmann, P., Harris, N.B., 2005. Linking Coniacian–Santonian (OAE3) Black-Shale Deposition to African Climate Variability: A Reference Section from the Eastern Tropical Atlantic at Orbital Time Scales (ODP Site 959, Off Ivory Coast and Ghana), The Deposition of Organic-Carbon-Rich Sediments: Models, Mechanisms, and Consequences. SEPM Society for Sedimentary Geology, pp. 125-143.

Bohacs, K., Jr, G.J., Carroll, A., 2007. Lithofacies architecture and variations in expression of sequence stratigraphy within representative intervals of the Green River Formation, Greater Green River Basin, Wyoming and Colorado. Mountain Geologist 44, 39-60.

Bohacs, K.M., 1998. Contrasting expressions of depositional sequences in mudrocks from marine to non marine environs. In: J. Schieber, W. Zimmerle, P.S. Sethi (Eds.), Shales and Mudstones I. Basin Studies, Sedimentology and Paleontology. Schweizerbart'sche Verlagsbuchhandlung, Stuttgart, pp. 32-77.

Bohacs, K.M., Carroll, A.R., Neal, J.E., Mankiewicz, P.J., Gierlowski-Kordesch, E.H., Kelts, K.R., 2000. Lake-Basin Type, Source Potential, and Hydrocarbon Character: an Integrated Sequence-Stratigraphic–Geochemical Framework, Lake Basins Through Space and Time. American Association of Petroleum Geologists, pp. 3-33.

Bohacs, K.M., Grabowski, G.J., Jr., Carroll, A.R., Mankiewicz, P.J., Miskell-Gerhardt, K.J., Schwalbach, J.R., Wegner, M.B., Simo, J.A., Harris, N.B., 2005. Production, Destruction, and Dilution—The Many Paths to Source-Rock Development, The Deposition of Organic-Carbon-Rich Sediments: Models, Mechanisms, and Consequences. SEPM Society for Sedimentary Geology, pp. 62-101.

Bohacs, K.M., Neal, J.E., Grabowski, G.J., Jr., Reynolds, D.J., Carroll, A.R., Armentrout, J.M., Rosen, N.C., 2002. Controls on Sequence Architecture in Lacustrine Basins—Insights for Sequence Stratigraphy in General. In: J.M. Armentrout, N.C. Rosen (Eds.), Sequence Stratigraphic Models for Exploration and Production: Evolving Methodology, Emerging Models and Application Histories. SEPM Society for Sedimentary Geology, pp. 403-423.

Boucot, A.J., Xu, C., Scotese, C.R., Morley, R.J., 2013. Phanerozoic Paleoclimate: An Atlas of Lithologic Indicators of Climate. SEPM CONCEPTS IN SEDIMENTOLOGY AND PALEONTOLOGY. SEPM Society for Sedimentary Geology.

Cai, Q., Hu, M., Ngia, N.R., Hu, Z., 2017. Sequence stratigraphy, sedimentary systems and implications for hydrocarbon exploration in the northern Xujiaweizi Fault Depression, Songliao Basin, NE China. Journal of Petroleum Science and Engineering 152, 471-494.

Cao, W., Lee, C.-T.A., Lackey, J.S., 2017. Episodic nature of continental arc activity since 750 Ma: A global compilation. Earth and Planetary Science Letters 461, 85-95.

Carroll, A.R., 1998. Upper Permian lacustrine organic facies evolution, Southern Junggar Basin, NW China. Organic Geochemistry 28, 649-667.

Carroll, A.R., Bohacs, K.M., 1999. Stratigraphic classification of ancient lakes: Balancing tectonic and climatic controls. Geology 27, 99-102.

Carroll, A.R., Bohacs, K.M., 2001. Lake-Type Controls on Petroleum Source Rock Potential in Nonmarine Basins. American Association of Petroleum Geologists Bulletin 85, 1033-1053.

Carroll, A.R., Brassell, S.C., Graham, S.A., 1992. Upper Permian Lacustrine Oil Shales, Southern Junggar Basin, Northwest China. American Association of Petroleum Geologists Bulletin 76, 1874-1902.

Catuneanu, O., 2022. Principles of Sequence Stratigraphy (Second Edition). Elsevier, Amsterdam, pp. 344-350.

Catuneanu, O., Abreu, V., Bhattacharya, J.P., Blum, M.D., Dalrymple, R.W., Eriksson, P.G., Fielding, C.R., Fisher, W.L., Galloway, W.E., Gibling, M.R., Giles, K.A., Holbrook, J.M., Jordan, R., Kendall, C.G.S.C., Macurda, B., Martinsen, O.J., Miall, A.D., Neal, J.E., Nummedal, D., Pomar, L., Posamentier, H.W., Pratt, B.R., Sarg, J.F., Shanley, K.W., Steel, R.J., Strasser, A., Tucker, M.E., Winker, C., 2009. Towards the standardization of sequence stratigraphy. Earth-Science Reviews 92, 1-33.

Catuneanu, O., Galloway, W.E., Kendall, C.G.S.C., Miall, A.D., Posamentier, H.W., Strasser, A., Tucker, M.E., 2011. Sequence Stratigraphy: Methodology and Nomenclature. Newsletters on Stratigraphy 44, 173-245.

Cox, R., Lowe, D.R., Cullers, R.L., 1995. The influence of sediment recycling and basement composition on evolution of mudrock chemistry in the southwestern United States. Geochimica et Cosmochimica Acta 59, 2919-2940.

Dean, W.E., Arthur, M.A., Claypool, G.E., 1986. Depletion of 13C in Cretaceous marine organic matter: Source, diagenetic, or environmental sigal? Marine Geology 70, 119-157.

Dean, W.E., Ethridge, F.G., Flores, R.M., 1981. Carbonate Minerals and Organic Matter in Sediments of Modern North Temperate Hard-Water Lakes, Recent and Ancient Nonmarine Depositional Environments: Models for Exploration. SEPM Society for Sedimentary Geology, pp. 213-231.

Deng, Q., Hu, M., Kane, O.I., Cai, Q., Hu, Z., Yang, W., 2021. Syn-rift sedimentary evolution and hydrocarbon reservoir models in a graben rift sag, Songliao Basin, Northeast China. Marine and Petroleum Geology 132, 105245.

Emerson, S., Hedges, J.I., 1988. Processes controlling the organic carbon content of open ocean sediments. Paleoceanography 3, 621-634.

Espitalie, J., Madec, M., Tissot, B., Mennig, J.J., Leplat, P., Source Rock Characterization Method for Petroleum Exploration. In, Offshore Technology Conference. 1977, OTC-2935-MS.

Espitalié, J., Marquis, F., Barsony, I., 1984. 9 - GEOCHEMICAL LOGGING. In: K.J. Voorhees (Ed.), Analytical Pyrolysis. Butterworth-Heinemann, pp. 276-304.

Fedo, C.M., Wayne Nesbitt, H., Young, G.M., 1995. Unraveling the effects of potassium metasomatism in sedimentary rocks and paleosols, with implications for paleoweathering conditions and provenance. Geology 23, 921-924.

Feng, Y., Li, S., Lu, Y., 2013. Sequence stratigraphy and architectural variability in Late Eocene lacustrine strata of the Dongying Depression, Bohai Bay Basin, Eastern China. Sedimentary Geology 295, 1-26.

Feng, Z.-q., Jia, C.-z., Xie, X.-n., Zhang, S., Feng, Z.-h., Cross, T.A., 2010. Tectonostratigraphic units and stratigraphic sequences of the nonmarine Songliao basin, northeast China. Basin Research 22, 79-95.

French, K.L., Birdwell, J.E., Lillis, P.G., 2022. Geochemistry of the Cretaceous Mowry Shale in the Wind River Basin, Wyoming. Geological Society of America Bulletin. doi: https://doi.org/10.1130/B36382.1

Gao, F., Song, Y., Li, Z., Xiong, F., Chen, L., Zhang, Y., Liang, Z., Zhang, X., Chen, Z., Joachim, M., 2018. Lithofacies and reservoir characteristics of the Lower Cretaceous continental Shahezi Shale in the Changling Fault Depression of Songliao Basin, NE China. Marine and Petroleum Geology 98, 401-421.

Hackley, P.C., Cardott, B.J., 2016. Application of organic petrography in North American shale petroleum systems: A review. International Journal of Coal Geology 163, 8-51.

Han, S., Xie, L., Du, X., Xiang, C., Huang, J., Tang, Z., Wang, C., Horsfield, B., Mahlstedt, N., 2023. Insights into organic metagenesis using Raman spectroscopy and high resolution mass spectrometry: A case study of the Shahezi formation, deep Songliao basin, China. International Journal of Coal Geology 265, 104153.

Hao, F., Zhou, X., Zhu, Y., Yang, Y., 2011. Lacustrine source rock deposition in response to co-evolution of environments and organisms controlled by tectonic subsidence and climate, Bohai Bay Basin, China. Organic Geochemistry 42, 323-339.

Harris, N.B., 2000. Evolution of the Congo rift basin, West Africa: an inorganic geochemical record in lacustrine shales. Basin Research 12, 425-445.

Harris, N. B., K. H. Freeman, R. D. Pancost, G. D. Mitchell, T. S. White, R. H. Bate, and N. B. Harris, 2005, Patterns of Organic-Carbon Enrichment in a Lacustrine Source Rock in Relation to Paleo–Lake Level, Congo Basin, West Africa, The

Deposition of Organic-Carbon-Rich Sediments: Models, Mechanisms, and Consequences, v. 82, SEPM Society for Sedimentary Geology, p. 102-123.

Harris, N.B., Freeman, K.H., Pancost, R.D., White, T.S., Mitchell, G.D., 2004. The character and origin of lacustrine source rocks in the Lower Cretaceous synrift section, Congo Basin, west Africa. American Association of Petroleum Geologists Bulletin 88, 1163-1184.

Harris, N.B., McMillan, J.M., Knapp, L.J., Mastalerz, M., 2018. Organic matter accumulation in the Upper Devonian Duvernay Formation, Western Canada Sedimentary Basin, from sequence stratigraphic analysis and geochemical proxies. Sedimentary Geology 376, 185-203.

Harris, N.B., Tucker, G.E., 2015. Soils, slopes and source rocks: Application of a soil chemistry model to nutrient delivery to rift lakes. Sedimentary Geology 323, 31-42.

Hasegawa, T., 1997. Cenomanian-Turonian carbon isotope events recorded in terrestrial organic matter from northern Japan. Palaeogeography, Palaeoclimatology, Palaeoecology 130, 251-273.

Hoefs, J., 2009. Isotope Fractionation Processes of Selected Elements. In: J. Hoefs (Ed.), Stable Isotope Geochemistry. Springer Berlin Heidelberg, Berlin, Heidelberg, pp. 35-92.

International Committee for Coal and Organic Petrology (ICCP), 1998. The new vitrinite classification (ICCP System 1994). Fuel 77, 349-358.

International Committee for Coal and Organic Petrology (ICCP), 2001. The new inertinite classification (ICCP System 1994). Fuel 80, 459-471.

Ji, Z., Meng, Q., Wan, C., Ge, W., Yang, H., Zhang, Y., Dong, Y., Jin, X., 2019. Early Cretaceous adakitic lavas and A-type rhyolites in the Songliao Basin, NE China: Implications for the mechanism of lithospheric extension. Gondwana Research 71, 28-48.

Jia, H., Ji, H., Wang, L., Yang, D., Meng, P., Shi, C., 2016. Tectono-sedimentary and hydrocarbon potential analysis of rift-related successions in the Dehui Depression, Songliao Basin, Northeastern China. Marine and Petroleum Geology 76, 262-278.

Jones, B., Manning, D.A.C., 1994. Comparison of geochemical indices used for the interpretation of palaeoredox conditions in ancient mudstones. Chemical Geology 111, 111-129.

Kagya, M., Ntomola, S.J., Mpanju, F., 1991. The source rock of the Nyasa Rift Basin and oil shows of Tanzania. Journal of Southeast Asian Earth Sciences 5, 407-419.

Katz, B.J., 1990. Controls on Distribution of Lacustrine Source Rocks through Time and Space, Lacustrine Basin Exploration: Case Studies and Modern Analogs. American Association of Petroleum Geologists, pp. 61-76.

Katz, B.J., 1995. A survey of rift basin source rocks. Geological Society, London, Special Publications 80, 213-240.

Katz, B.J., 2005. Controlling Factors on Source Rock Development—A Review of Productivity, Preservation, and Sedimentation Rate, The Deposition of Organic-Carbon-Rich Sediments: Models, Mechanisms, and Consequences. SEPM Society for Sedimentary Geology, pp. 7-16.

Kelts, K., 1988. Environments of deposition of lacustrine petroleum source rocks: an introduction. Geological Society, London, Special Publications 40, 3-26.

Kleinspehn, K.L., Steel, R.J., Johannessen, E., Netland, A., 1984. Conglomeratic fan-delta sequences, Late Carboniferous-Early Permian, western Spitsbergen. In: E.H. Koster, R.J. Steel (Eds.), Sedimentology of gravels and conglomerates. Memoir - Canadian Society of Petroleum Geologists. Canadian Society of Petroleum Geologists, Calgary, AB, Canada, Calgary, AB, Canada, pp. 279-294.

Lambiase, J.J., Katz, B.J., 1990. A Model for Tectonic Control of Lacustrine Stratigraphic Sequences in Continental Rift Basins, Lacustrine Basin Exploration: Case Studies and Modern Analogs. American Association of Petroleum Geologists, pp. 265-276.

Langford, F.F., Blanc-Valleron, M.M., 1990. Interpreting Rock-Eval pyrolysis data using graphs of pyrolizable hydrocarbons vs. total organic carbon. American Association of Petroleum Geologists Bulletin 74, 799-804.

Lawrence, D.T., Doyle, M., Aigner, T., 1990. Stratigraphic Simulation of Sedimentary Basins: Concepts and Calibration1. American Association of Petroleum Geologists Bulletin 74, 273-295.

Lazar, O.R., Bohacs, K.M., Macquaker, J.H.S., Schieber, J., Demko, T.M., 2015. Capturing Key Attributes of Fine-Grained Sedimentary Rocks In Outcrops, Cores, and Thin Sections: Nomenclature and Description Guidelines. Journal of Sedimentary Research 85, 230-246.

Lin, C., Kenneth, E., Li, S., Wan, Y., Ren, J., Zhang, Y., 2001. Sequence Architecture, Depositional Systems, and Controls on Development of Lacustrine Basin Fills in Part of the Erlian Basin, Northeast China. American Association of Petroleum Geologists Bulletin 85, 2017-2043.

Liu, B., Mastalerz, M., Schieber, J., 2022a. SEM petrography of dispersed organic matter in black shales: A review. Earth-Science Reviews 224, 103874.

Liu, B., Schieber, J., Mastalerz, M., 2017. Combined SEM and reflected light petrography of organic matter in the New Albany Shale (Devonian-Mississippian) in the Illinois Basin: A perspective on organic pore development with thermal maturation. International Journal of Coal Geology 184, 57-72.

Liu, B., Schieber, J., Mastalerz, M., Camp, W.K., Milliken, K.L., Taylor, K., Fishman, N., Hackley, P.C., Macquaker, J.H.S., 2019a. Petrographic and Micro-FTIR Study of Organic Matter in the Upper Devonian New Albany Shale During Thermal Maturation: Implications for Kerogen Transformation, Mudstone Diagenesis: Research Perspectives for Shale Hydrocarbon Reservoirs, Seals, and Source Rocks. The American Association of Petroleum Geologists, pp. 165-188.

Liu, B., Schieber, J., Mastalerz, M., Teng, J., 2019b. Organic matter content and type variation in the sequence stratigraphic context of the Upper Devonian New Albany Shale, Illinois Basin. Sedimentary Geology 383, 101-120.

Liu, H., Wang, P., Gao, Y., Hou, H., Yin, Y., Li, H., Feng, Y., 2021. New data from ICDP borehole SK2 and its constraint on the beginning of the Lower Cretaceous Shahezi Formation in the Songliao Basin, NE China. Science Bulletin 66, 411-413.

Liu, W., Liu, M., Yang, T., Liu, X., Them, T.R., Wang, K., Bian, C., Meng, Q.a., Li, Y., Zeng, X., Zhao, W., 2022b. Organic matter accumulations in the Santonian-Campanian (Upper Cretaceous) lacustrine Nenjiang shale (K2n) in the Songliao Basin, NE China: Terrestrial responses to OAE3? International Journal of Coal Geology 260, 104069.

Ma, Y., Fan, M., Lu, Y., Liu, H., Hao, Y., Xie, Z., Liu, Z., Peng, L., Du, X., Hu, H., 2016. Climate-driven paleolimnological change controls lacustrine mudstone depositional process and organic matter accumulation: Constraints from lithofacies and geochemical studies in the Zhanhua Depression, eastern China. International Journal of Coal Geology 167, 103-118.

Mastalerz, M., Drobniak, A., Stankiewicz, A.B., 2018. Origin, properties, and implications of solid bitumen in source-rock reservoirs: A review. International Journal of Coal Geology 195, 14-36.

Martins-Neto, M.A., Catuneanu, O., 2010. Rift sequence stratigraphy. Marine and Petroleum Geology 27, 247-253.

McLennan, S.M., 1993. Weathering and Global Denudation. The Journal of Geology 101, 295-303.

Mendonça, R., Müller, R.A., Clow, D., Verpoorter, C., Raymond, P., Tranvik, L.J., Sobek, S., 2017. Organic carbon burial in global lakes and reservoirs. Nature Communications 8, 1694.

Meng, Q.-R., Zhou, Z.-H., Zhu, R.-X., Xu, Y.-G., Guo, Z.-T., 2021. Cretaceous basin evolution in northeast Asia: Tectonic responses to the paleo-Pacific plate subduction. National Science Review 9, nwab088.

Meyers, P.A., 1994. Preservation of elemental and isotopic source identification of sedimentary organic matter. Chemical Geology 114, 289-302.

Meyers, P.A., Bernasconi, S.M., Forster, A., 2006. Origins and accumulation of organic matter in expanded Albian to Santonian black shale sequences on the Demerara Rise, South American margin. Organic Geochemistry 37, 1816-1830.

Meyers, P.A., Ishiwatari, R., 1993. The Early Diagenesis of Organic Matter in Lacustrine Sediments. In: M.H. Engel, S.A. Macko (Eds.), Organic Geochemistry: Principles and Applications. Springer US, Boston, MA, pp. 185-209.

Meyers, P.A., Lallier-vergés, E., 1999. Lacustrine Sedimentary Organic Matter Records of Late Quaternary Paleoclimates. Journal of Paleolimnology 21, 345-372.

Moore, D.M., Reynolds, R.C., Jr., 1989. X-ray diffraction and the identification and analysis of clay minerals. Oxford University Press (OUP), Oxford.

Ndip, E.A., Agyingi, C.M., Nton, M.E., Hower, J.C., Oladunjoye, M.A., 2019. Organic petrography and petroleum source rock evaluation of the Cretaceous Mamfe Formation, Mamfe basin, southwest Cameroon. International Journal of Coal Geology 202, 27-37.

Nelson, C.H., Karabanov, E.B., Colman, S.M., Escutia, C., 1999. Tectonic and sediment supply control of deep rift lake turbidite systems: Lake Baikal, Russia. Geology 27, 163-166.

Nesbitt, H.W., Young, G.M., 1982. Early Proterozoic climates and plate motions inferred from major element chemistry of lutites. Nature 299, 715-717.

Nesbitt, H.W., Young, G.M., 1984. Prediction of some weathering trends of plutonic and volcanic rocks based on thermodynamic and kinetic considerations. Geochimica et Cosmochimica Acta 48, 1523-1534.

Nesbitt, H.W., Young, G.M., 1989. Formation and Diagenesis of Weathering Profiles. The Journal of Geology 97, 129-147.

Ogrinc, N., Fontolan, G., Faganeli, J., Covelli, S., 2005. Carbon and nitrogen isotope compositions of organic matter in coastal marine sediments (the Gulf of Trieste, N Adriatic Sea): indicators of sources and preservation. Marine Chemistry 95, 163-181.

Oliver, G.M., Ly, C.V., Spence, G., Rael, H., A New Approach to Measuring Rock Properties Data from Cores & Cuttings for Reservoir & Completions Characterization: an Example from the Bakken Formation. In, SPE Unconventional Resources Conference and Exhibition-Asia Pacific. 2013, SPE-166997-MS.

Olsen, P.E., Katz, B.J., 1990. Tectonic, Climatic, and Biotic Modulation of Lacustrine Ecosystems—Examples from Newark Supergroup of Eastern North America, Lacustrine Basin Exploration: Case Studies and Modern Analogs. American Association of Petroleum Geologists, pp. 209-224.

Olsen, P.E., Kent, D.V., Cornet, B., Witte, W.K., Schlische, R.W., 1996. High-resolution stratigraphy of the Newark rift basin (early Mesozoic, eastern North America). Geological Society of America Bulletin 108, 40-77.

Pan, A., 2020. Rock-Eval testing report. 19-583-124, Experimental research center of Wuxi research institute of petroleum geology of SINOPEC, Wuxi, China.

Panahi, A., Young, G.M., 1997. A geochemical investigation into the provenance of the Neoproterozoic Port Askaig Tillite, Dalradian Supergroup, western Scotland. Precambrian Research 85, 81-96.

Panahi, A., Young, G.M., Rainbird, R.H., 2000. Behavior of major and trace elements (including REE) during Paleoproterozoic pedogenesis and diagenetic alteration of an Archean granite near Ville Marie, Québec, Canada. Geochimica et Cosmochimica Acta 64, 2199-2220.

Passey, Q.R., Bohacs, K.M., Esch, W.L., Klimentidis, R., Sinha, S., From Oil-Prone Source Rock to Gas-Producing Shale Reservoir – Geologic and Petrophysical Characterization of Unconventional Shale-Gas Reservoirs. In, International Oil and Gas Conference and Exhibition in China. 2010, SPE-131350-MS.

Pedernera, T.E., Ottone, E.G., Mancuso, A.C., Erra, G., Larriestra, F., Benavente, C.A., Pineda Alvarez, J.A., Campos, C., Bustos Escalona, E.L., Krapovickas, V., Marsicano, C.A., 2021. Multiproxy analyses of the Triassic Agua de la Zorra Formation, Cuyana Basin, Argentina: Palynofacies, geochemistry, and biotic record. Journal of South American Earth Sciences 110, 103374.

Pedersen, T.F., Calvert, S.E., 1990. Anoxia vs. Productivity: What Controls the Formation of Organic-Carbon-Rich Sediments and Sedimentary Rocks?1. American Association of Petroleum Geologists Bulletin 74, 454-466.

Peters, K.E., 1986. Guidelines for Evaluating Petroleum Source Rock Using Programmed Pyrolysis1. American Association of Petroleum Geologists Bulletin 70, 318-329.

Petersen, H.I., Bojesen-Koefoed, J.A., Mathiesen, A., 2010. VARIATIONS IN COMPOSITION, PETROLEUM POTENTIAL AND KINETICS OF ORDOVICIAN – MIOCENE TYPE I AND TYPE I-II SOURCE ROCKS (OIL SHALES):

IMPLICATIONS FOR HYDROCARBON GENERATION CHARACTERISTICS. Journal of Petroleum Geology 33, 19-41.

Picarelli, A., Abreu, V., Baganz, O.W., Bartov, Y., Bohacs, K.M., Nummedal, D., 2012. Sequence Stratigraphy Applied to Continental Rift Basins: Example from Recôncavo Basin, Brazil, Lacustrine Sandstone Reservoirs and Hydrocarbon Systems. American Association of Petroleum Geologists, pp. 347-366.

Pietras, J.T., Carroll, A.R., 2006. High-Resolution Stratigraphy of an Underfilled Lake Basin: Wilkins Peak Member, Eocene Green River Formation, Wyoming, U.S.A. Journal of Sedimentary Research 76, 1197-1214.

Piper, D.Z., Calvert, S.E., 2009. A marine biogeochemical perspective on black shale deposition. Earth-Science Reviews 95, 63-96.

Posamentier, H.W., Jervey, M.T., Vail, P.R., Wilgus, C.K., Hastings, B.S., Posamentier, H., Wagoner, J.V., Ross, C.A., Kendall, C.G.S.C., 1988. Eustatic Controls on Clastic Deposition I—Conceptual Framework, Sea-Level Changes: An Integrated Approach. SEPM Society for Sedimentary Geology, pp. 109-124.

Posamentier, H.W., Vail, P.R., Wilgus, C.K., Hastings, B.S., Posamentier, H., Wagoner, J.V., Ross, C.A., Kendall, C.G.S.C., 1988. Eustatic Controls on Clastic Deposition II—Sequence and Systems Tract Models, Sea-Level Changes: An Integrated Approach. SEPM Society for Sedimentary Geology, pp. 125-154.

Powell, T.G., 1986. Petroleum geochemistry and depositional setting of lacustrine source rocks. Marine and Petroleum Geology 3, 200-219.

Regnier, P., Resplandy, L., Najjar, R.G., Ciais, P., 2022. The land-to-ocean loops of the global carbon cycle. Nature 603, 401-410.

Sageman, B.B., Murphy, A.E., Werne, J.P., Ver Straeten, C.A., Hollander, D.J., Lyons, T.W., 2003. A tale of shales: the relative roles of production, decomposition, and dilution in the accumulation of organic-rich strata, Middle–Upper Devonian, Appalachian basin. Chemical Geology 195, 229-273.

Sanei, H., 2020. Genesis of solid bitumen. Scientific Reports 10, 15595.

Sarki Yandoka, B.M., Abdullah, W.H., Abubakar, M.B., Adegoke, A.K., Maigari, A.S., Haruna, A.I., Yaro, U.Y., 2017. Hydrocarbon potential of Early Cretaceous lacustrine sediments from Bima Formation, Yola Sub-basin, Northern Benue Trough, NE Nigeria: Insight from organic geochemistry and petrology. Journal of African Earth Sciences 129, 153-164.

Schlünz, B., Schneider, R.R., 2000. Transport of terrestrial organic carbon to the oceans by rivers: re-estimating flux- and burial rates. International Journal of Earth Sciences 88, 599-606.

Scotese, C., 2016. Global Climate Change (Modern Times to 540 million years ago).

Shanley, K.W., McCabe, P.J., 1994. Perspectives on the Sequence Stratigraphy of Continental Strata. American Association of Petroleum Geologists Bulletin 78, 544-568.

Singer, A., 1980. The paleoclimatic interpretation of clay minerals in soils and weathering profiles. Earth-Science Reviews 15, 303-326.

Smyth, M., Mastalerz, M., 1991. Organic petrological composition of Triassic source rocks and their clastic depositional environments in some Australian sedimentary basins. International Journal of Coal Geology 18, 165-186.

Snyder, R.L., 1992. The Use of Reference Intensity Ratios in X-Ray Quantitative Analysis. Powder Diffraction 7, 186-193.

Sobek, S., Durisch-Kaiser, E., Zurbrügg, R., Wongfun, N., Wessels, M., Pasche, N., Wehrli, B., 2009. Organic carbon burial efficiency in lake sediments controlled by oxygen exposure time and sediment source. Limnology and Oceanography 54, 2243-2254.

Sohn, Y.K., 2000. Depositional Processes of Submarine Debris Flows in the Miocene Fan Deltas, Pohang Basin, SE Korea with Special Reference to Flow Transformation. Journal of Sedimentary Research 70, 491-503.

Soreghan, M.J., Scholz, C.A., Wells, J.T., 1999. Coarse-grained, deep-water sedimentation along a border fault margin of Lake Malawi, Africa; seismic stratigraphic analysis. Journal of Sedimentary Research 69, 832-846.

Sweeney, J.J., Burnham, A.K., 1990. Evaluation of a Simple Model of Vitrinite Reflectance Based on Chemical Kinetics1.

American Association of Petroleum Geologists Bulletin 74, 1559-1570.

Taylor, S.R., McLennan, S.M., 1985. The Continental Crust: Its Composition and Evolution. Geoscience texts. Blackwell Scientific, Oxford.

Tissot, B.P., Welte, D.H., 1984. Petroleum Formation and Occurrence. Springer-Verlag Berlin Heidelberg.

Tong, X., Hu, J., Xi, D., Zhu, M., Song, J., Peng, P.a., 2018. Depositional environment of the Late Santonian lacustrine source rocks in the Songliao Basin (NE China): Implications from organic geochemical analyses. Organic Geochemistry 124, 215-227.

Tranvik, L.J., Downing, J.A., Cotner, J.B., Loiselle, S.A., Striegl, R.G., Ballatore, T.J., Dillon, P., Finlay, K., Fortino, K., Knoll, L.B., Kortelainen, P.L., Kutser, T., Larsen, S., Laurion, I., Leech, D.M., McCallister, S.L., McKnight, D.M., Melack, J.M., Overholt, E., Porter, J.A., Prairie, Y., Renwick, W.H., Roland, F., Sherman, B.S., Schindler, D.W., Sobek, S., Tremblay, A., Vanni, M.J., Verschoor, A.M., von Wachenfeldt, E., Weyhenmeyer, G.A., 2009. Lakes and reservoirs as regulators of carbon cycling and climate. Limnology and Oceanography 54, 2298-2314.

Tyson, R.V., 2001. Sedimentation rate, dilution, preservation and total organic carbon: some results of a modelling study. Organic Geochemistry 32, 333-339.

Tyson, R.V., 2005. The “Productivity Versus Preservation” Controversy: Cause, Flaws, and Resolution, The Deposition of Organic-Carbon-Rich Sediments: Models, Mechanisms, and Consequences. SEPM Society for Sedimentary Geology, pp. 17-33.

van Koeverden, J.H., Karlsen, D.A., Backer-Owe, K., 2011. CARBONIFEROUS NON-MARINE SOURCE ROCKS FROM SPITSBERGEN AND BJØRNØYA: COMPARISON WITH THE WESTERN ARCTIC. Journal of Petroleum Geology 34, 53-66.

von Eynatten, H., Barceló-Vidal, C., Pawlowsky-Glahn, V., 2003. Modelling Compositional Change: The Example of Chemical Weathering of Granitoid Rocks. Mathematical Geology 35, 231-251.

Wang, C., Zhang, M., Sun, K., Wang, Y., Li, X., Liu, X., 2017a. Latest Zircon U-Pb Geochronology of the Huoshiling Formation Volcanic Rocks in the Southeastern Margin of the Songliao Basin. Acta Geologica Sinica - English Edition 91, 1924-1925.

Wang, H., Fan, T., Li, R., Hou, Y., Fan, X., Zhang, B., 2017b. Search for hydrocarbon traps in syncline structures: A case study from the Lishu Depression of Songliao Basin, China. Journal of Petroleum Science and Engineering 159, 76-91.

Wang, H., Li, R., Zhu, J., Yang, X., 2021. Origin and evolution of unconformities in a continental rift basin: a case study from the Lishu Depression in Songliao Basin, China. Canadian Journal of Earth Sciences 58, 1085-1102.

Wang, P.-J., Mattern, F., Didenko, N.A., Zhu, D.-F., Singer, B., Sun, X.-M., 2016. Tectonics and cycle system of the Cretaceous Songliao Basin: An inverted active continental margin basin. Earth-Science Reviews 159, 82-102.

Wang, Q., Li, Y., 2023. Rock-Eval analysis of the Lower Cretaceous (Middle Aption-Early Albian) Shahezi Formation in the Xujiaweizi Rift Depression, Songliao Basin, NE Asia. Mendeley Data, v1. http://dx.doi.org/10.17632/82fvmc2vyp.1

Wang, Q., Yang, W., Li, Y., Jiang, Z., Wen, M., Zuo, R., Wang, X., Xue, Z., Wang, Y., 2023. In-situ fluid phase variation along the thermal maturation gradient in shale petroleum system and its impact on well production performance. Journal of Earth Science, in press.

Wedepohl, K.H., 1971. Environmental influences on the chemical composition of shales and clays. Physics and Chemistry of the Earth 8, 307-333.

White, A.F., Blum, A.E., 1995. Effects of climate on chemical_ weathering in watersheds. Geochimica et Cosmochimica Acta 59, 1729-1747.

Wood, M.L., Ethridge, F.G., 1988. Sedimentology and architecture of Gilbert- and mouth bar-type fan deltas, Paradox Basin, Colorado; Sédimentologie et architecture d'éventails deltaïques de type Gilbert et de barre d'embouchure du bassin Paradox au Colorado, Fan deltas : sedimentology and tectonic settings. Blackie, London, pp. 251-263.

Xu, X., Zhang, J., Liu, W., Bai, J., Chen, S., Li, Y., Liu, C., Liu, X., Zhang, J., Hu, Z., Li, H., Sun, J., Zhang, S., Wu, Z., 2020a. The continental shale gas investigation in southern Songliao Basin. Shale gas resource exploration in the Southern Songliao Basin (Grant No. DD20190115), China Geological Survey, Beijing, China.

Xu, Z., Wang, Y., Jiang, S., Fang, C., Liu, L., Wu, K., Luo, Q., Li, X., Chen, Y., 2022. Impact of input, preservation and dilution on organic matter enrichment in lacustrine rift basin: A case study of lacustrine shale in Dehui Depression of Songliao Basin, NE China. Marine and Petroleum Geology 135, 105386.

Xu, X.-T., Shao, L.-Y., Lan, B., Wang, S., Hilton, J., Qin, J.-Y., Hou, H.-H., Zhao, J., 2020b. Continental chemical weathering during the Early Cretaceous Oceanic Anoxic Event (OAE1b): a case study from the Fuxin fluvio-lacustrine basin, Liaoning Province, NE China. Journal of Palaeogeography 9, 12.

Yan, W., Fan, T., Wang, H., Zhu, C., Gao, Z., Meng, X., Sun, Y., Yang, F., 2017. Micropaleontology and palaeoclimate during the early Cretaceous in the Lishu depression, Songliao basin, Northeast China. Geoscience Frontiers 8, 93-106.

Yang, D., 2019. Depositional environment of the muddy shales in the Shahezi Formation, Changling Fault Depression, NE China (Msc degree thesis), China University of Petroleum (Beijing), Beijing, China.

Yang, W., Wang, Q., Wang, Y., Jiang, Z., Song, Y., Li, Y., Liu, D., Zuo, R., Gu, X., Zhang, F., 2020. Pore characteristic responses to categories of depositional microfacies of delta-lacustrine tight reservoirs in the Upper Triassic Yanchang Formation, Ordos Basin, NW China. Marine and Petroleum Geology, 118, 104423.

Yang, W., Zuo, R., Chen, D., Jiang, Z., Guo, L., Liu, Z., Chen, R., Zhang, Y., Zhang, Z., Song, Y., Luo, Q., Wang, Q., Wang, J., Chen, L., Li, Y., Zhang, C., 2019. Climate and tectonic-driven deposition of sandwiched continental shale units: New insights from petrology, geochemistry, and integrated provenance analyses (the western Sichuan subsiding Basin, Southwest China). International Journal of Coal Geology 211, 103227.

Yu, Z., He, H., Deng, C., Lu, K., Shen, Z., Li, Q., 2020. New SIMS U-Pb geochronology for the Shahezi Formation from CCSD-SK-IIe borehole in the Songliao Basin, NE China. Science Bulletin 65, 1049-1051.

Zhu, G., Jiang, D., Zhang, B., Chen, Y., 2012a. Destruction of the eastern North China Craton in a backarc setting:

Evidence from crustal deformation kinematics. Gondwana Research 22, 86-103.

Zhu, R., Xu, Y., Zhu, G., Zhang, H., Xia, Q., Zheng, T., 2012b. Destruction of the North China Craton. Science China Earth Sciences 55, 1565-1587.

FIGURE CAPTION

Fig. 1. Schematic diagram highlighting major features of syn-rift to post-rift lake basins: clastic and carbonate sedimentation, a mixed OC source of land plants and aquatic organisms, hydrocarbon phases, and decreased OC quantity along with burial diagenesis and thermal maturation.

Fig. 2. Tectonic and climatic controls on the OC enrichment of intracontinental lacustrine sediments highlighting the terrestrial OC production and input.

Fig. 3. (A) The tectonic location of Songliao Basin in northeastern Asia; (B) The tectonic units of the Songliao Basin and the location of Lishu Rift Depression; (C) The sub-tectonic units of Lishu Rift Depression, the location of boreholes; (D) The generalized tectonic basin filling stage (Wang et al., 2016), basin filling sequence and lithologies (Cai et al., 2017; Ji et al., 2019), sedimentary cycles and settings (Wang et al., 2016) and basin type variation (Feng et al., 2010). The zircon $^{206}Pb/^{238}U$ ages of Yingcheng Formation (Ji et al., 2019), Shahezi Formation (Yu et al., 2020; Liu et al., 2021), and Huoshiling Formation (Wang et al., 2017a) were attached to the lithology column.

Fig. 4. (A) A burial and thermal history of the Shahezi Formation from well SN17 (modified after Xu et al., 2020a). The location of well SN17 is marked in Fig. 3C. (B) A comparison of measured vitrinite reflectance values (points, from Xu et al., 2020a) and modeled EASY%Ro data (trend line, a simplified vitrinite maturation model proposed by Sweeney and Burnham, 1990).

Fig. 5. (A) A well-log cross section (See Fig. 3C for borehole locations) showing sequence stratigraphy of the Shahezi Formation in the Lishu Rift Depression, Songliao Basin; (B) Simplified interpretation of seismic reflection profile correlating the four wells in Fig. 5A; (C) A paleogeographic map showing the dominant depositional facies

and the well locations with respect to the fan-delta and lake in the Lishu Rift Depression during the Shahezi Formation. This map is created based on the spatial distribution of dominant sedimentary facies (Xu et al., 2020a) and a 3D image of the seismic RMS (root-mean-square) amplitude (Wang et al., 2017b).

Fig. 6. (A) Vertical distributions of lithologies, fan delta-lacustrine facies, stratal stacking, parasequence and sequence development of the Shahezi Formation recovered by well JLYY1. Subfacies: 1 = subaqueous channel fill, 2 = subaqueous interchannel deposits, 3 = mouth bar, 4 = pro-fan delta, 5 = shallow-littoral lake, 6 = sublacustrine fan, 7 = sublittoral-profundal lake. (B–H) typical lithologies and sedimentary structures of different depositional facies. (I) RoqSCAN SEM-EDS mineral map overlain on the SEM backscatter image to reveal the rock texture and mineral composition of the sublacustrine fan sample in Fig. 6H. Scale bar = 1 cm. The locations of all samples are marked in Figs. 5 and 6A.

Fig. 7. Measured section of the lacustrine-dominated interval from the Shahezi Formation, illustrating the distribution of depositional subfacies, TOC, shale/mudstone lithologies, stratal stacking, and parasequence development in an over-filled rift lake basin.

Fig. 8. Core photographs (A–E, G–I, K–L), high-resolution mineral maps (F), and large-area FIB-SEM image (J) of the lacustrine-dominated interval from the Shahezi Formation, illustrating the typical sedimentary structures, rock textures, mineral compositions, and organic matters of syn-rift lake sediments. Scale bar = 1 cm. See Fig. 7 for the sample location.

Fig. 9. The core photographs, backscatter SEM images, and RoqSCAN SEM-EDS mineral maps of the laminated shales deposited in the HST-1 (A) and TST-1 (B–D) sequences of the Shahezi Formation. See Fig. 10 for the mineral color scheme of RoqSCAN SEM-EDS. Ternary plots show the TOC concentrations, mineral compositions, and shale/mudstone lithofacies classification of the HST-1 (E) and TST-1 (F) sequences. See Fig. 7 for the sample location.

Fig. 10. The core photographs, backscatter SEM images, and RoqSCAN SEM-EDS mineral maps of the massive mudstones deposited in the HST-3 (A, B) and HST-2 (C, D) sequences of the Shahezi Formation. Ternary plots

show the TOC concentrations, mineral compositions, and shale/mudstone lithofacies classification of the HST-3 (E) and HST-2 (F) sequences. See Fig. 7 for the sample location.

Fig. 11. Air-dried (colored solid lines) and ethylene glycol (EG)-solved (black dash lines) X-ray diffractograms of five representative Shahezi Formation samples from JLYY1 borehole. Abbreviations: Ilt (illite), Mus (muscovite), Chl (chlorite), Q (quartz), I/S (interstratified illite/smectite), Kln (kaolinite). Diffractograms are presented in their unprocessed state, as acquired with automated divergence slits.

Fig. 12. SEM images of a laminated profundal shale sample from the Shahezi Formation (3154.0 m, Ro = 1.39%). (A) Backscatter SEM images and EDS spectrums of kaolinite- and illite-riched matrix; (B) Secondary electron image showing the broken chlorite blades and euhedral quartz crystallites in solid bitumen; (C, E) Backscatter SEM images of the solid bitumen-chlorite-quartz micro complex. (D) and (F) are secondary electron images showing the enlarged parts of (C) and (E), respectively. Abbreviations: Bt (biotite), Chl (chlorite), Fsp (feldspar), Ilt (illite), Kln (kaolinite), Qz (quartz), SB (solid bitumen).

Fig. 13. The total organic carbon content (TOC), hydrogen index (HI), and vitrinite reflectance data (R_o) of source rock samples from the JLYY1 borehole. The lacustrine-dominated invertal of Shahezi Formation is marked by grey color.

Fig. 14. (A) A cross-plot of T_{max} versus Hydrogen Index (HI) for lacustrine shales and mudstones from Shahezi Formation (adapted from Espitalié et al. (1984)); (B) A box-plot showing the HI variation as a function of different systems tracts. N and M represent the numbers and average values, respectively; (C) A cross-plot of S_2 versus %TOC to identify kerogen types. The HI threshold values for kerogen type classification are referenced from Langford and Blanc-Valleron (1990) and van Koeverden et al. (2011); (D) A cross-plot of the organic carbon isotopic composition ($\delta^{13}C_{org}$, ‰, VPDB) vs. %TOC of the Shahezi Formation. Molar ratios of TOC to total nitrogen (TOC/TN) are attached to help reveal the origins of organic matter.

Fig. 15. Combined reflected light (A–F) and SEM petrography (C–I) of organic macerals within the Shahezi Formation. The silt-size vitrinite and inertinite occur as subrounded to rounded granular particles or elongated bands, and do not host secondary organic pores (A–F). The inertinite particles have higher brightness of reflective

light than vitrinite (B) and their cellular structure derived from land plant material can be well preserved in subaqueous interchannel silty mudstones (G). The porous solid bitumen fills the inter-particle spaces between quartz and chlorite crystals (C, D, and H). Bivalve shell fragments and organic linings of foraminifera are also present in the Shahezi Formation shales (H). Abbreviations: Vit (vitrinite), Int (inertinite), SB (solid bitumen), Zls (zooclasts), Chl (chlorite), Qz (quartz).

Fig. 16. Gammay ray (GR, API) and acoustic (DT, μs/m) logs, pyrite and total carbonate concentrations (%), depositional subfacies (see Fig. 6 caption for the meaning of subfacies ranks 1–7), organic matter concentrations (%TOC), and hydrogen index (HI, mg HC/g C_{org}) of the Shahezi Formation shales and mudstones.

Fig. 17. Ternary diagrams of molecular proportions of Al_2O_3, CaO^*+Na_2O, K_2O and associated chemical index of alteration (CIA and CIA_{corr}). Solid symbols are the four systems tracts (TST-1, HST-1, HST-2, HST-3) of the Shahezi Formation. Hollow stars represent the Post-Archean Australian Shale (1-PAAS) (Taylor and McLennan, 1985), global Average Shale (2-AS) (Wedepohl, 1971), and other fresh silicate minerals and igneous rocks (3–12) (Fedo et al., 1995). Some idealized mineral compositions are also plotted (Ka: kaolinite, Chl: chlorite, Gi: gibbsite, Sm: smectite, Ill: illite, Mu: muscovite, Bt: biotite, Kfs: K-feldspar, Pl: plagioclase, Hbl: hornblende, Cpx: clinopyroxenel). The chemical weathering, potassium metasomatism and retrograde alteration paths (solid lines a–e) are also shown on the diagrams.

Fig. 18. Organic matter concentration (%TOC), compositional variation (ICV), nutrient input (P/Ti), and chemical weathering (CIA, CIA_{corr}, and $Ln(Al_2O_3/Na_2O)$) indices of shales and mudstones from Shahezi Formation. The red numbers of 0.28 and 1.85 indicate the chemical composition of global Average Shale (Wedepohl, 1971).

Fig. 19. Depositional models of the shales and mudstones from Shahezi Formation, showing the lacustrine OC burial induced by changes in rift sequence, chemical weathering, terrestrial OC input, and volcanism. See text for detailed discussion. The 2σ confidence intervals and mean values of TOC, HI, and CIA dataset are estimated using the Bootstrap Smoothing included in the *Acycle* software package (Li et al., 2019)

Fig. 20. (A) Early Cretaceous paleogeographic reconstruction (Aptian, 116 Ma) showing the global paleoclimate conditions (Boucot et al., 2013; Scotese, 2016; Cao et al., 2017). Positions of typical Lower Cretaceous shale

sequences deposited in the lacustrine rift basins are indicated by red points. The JLYY1 and International Continental Scientific Drilling Program (ICDP) SK-II boreholes represent the location of Middle Aptian-Early Albian (118 to 111 Ma) Shahezi Formation shales from the Songliao Basin, NE Asia. The YWC section and A-1 borehole represent the Santonian Nenjiang Formation shales in the Songliao Basin. The VIM-1 borehole (Harris, 2000; Harris et al., 2004) marks the Aptian (125 to 113 Ma) Sialivakou-Argilles Vertes Formations in the Congo Basin, western Africa. Purple and red lines indicate the internal and external continental arcs, respectively (Cao et al., 2017). Abbreviations of continental arcs: Ant: Antarctic Peninsula; Gd: Gangdese; ICS: Indochina–Sumatra; JK: Jiangda–Hoh Xil Shan–Karakorum; NA: North American Cordilleran; OC: Okhotsk–Chukotka; SA: South American Cordilleran; WP: West Pacific. (B–C) Cross-plots of CIA_{corr} vs. %TOC of shales and mudstones from Shahezi Formation (data from this study and Yang (2019)), Nenjiang (Liu et al., 2022b), and Sialivakou–Argilles Vertes Formations (Harris, 2000; Harris et al., 2004); (D–F) Cross-plots of Oxygen Index versus Hydrogen Index for shales and mudstones from Shahezi (Wang and Li, 2023; Han et al., 2023), Nenjiang (Tong et al., 2018), and Sialivakou–Argilles Vertes Formations (Harris, 2000; Harris et al., 2004).

Graphical Abstract

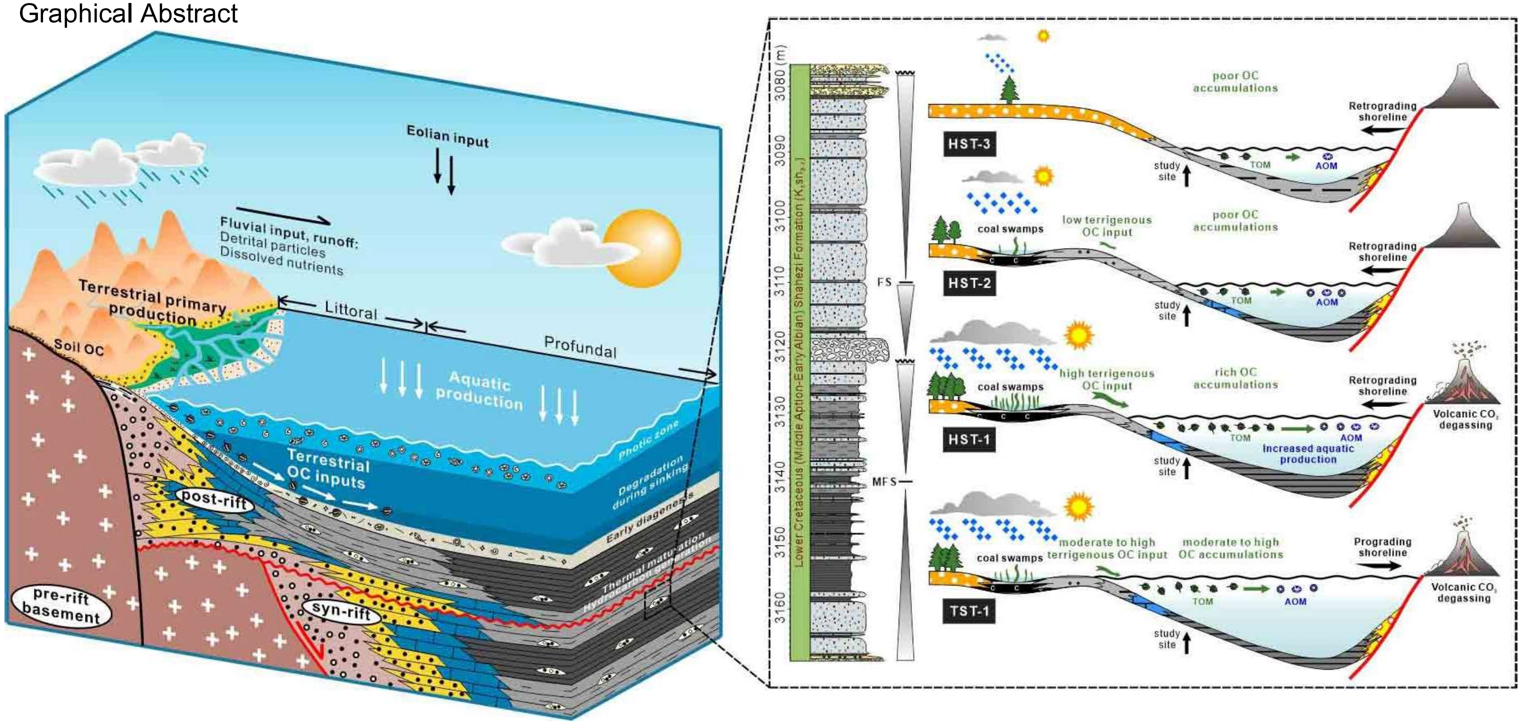

HIGHLIGHTS

- Multiple independent proxies revealed OC types and sources of highly mature shales.
- Terrestrial OC dominates the profundal shales in an Early Cretaceous syn-rift lake.
- Origin and content of lacustrine OC vary with rift sequence and paleoclimate changes.
- Application of a bioproductivity-based model in syn-rift lakes need to be questioned.

Figure 1

Click here to access/download;Figure;Figure 1.pdf

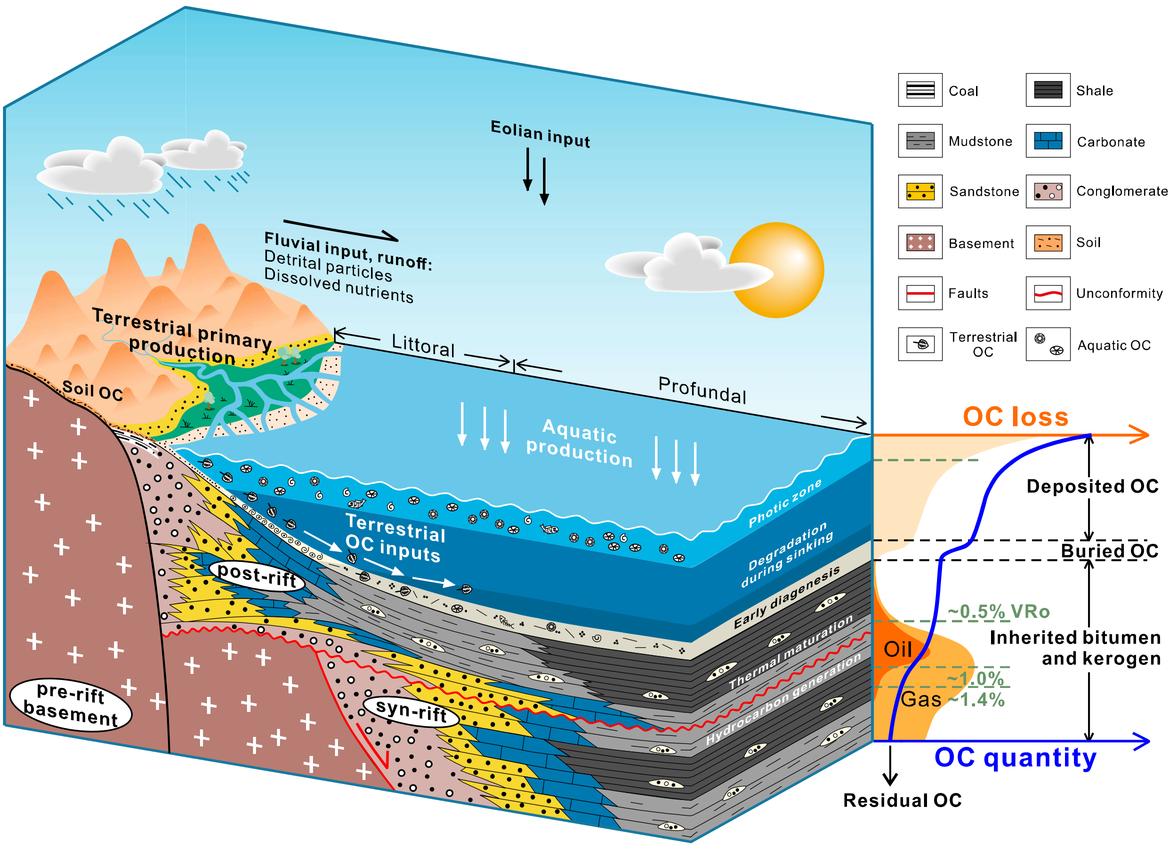

Figure 2

Click here to access/download;Figure;Figure 2.pdf

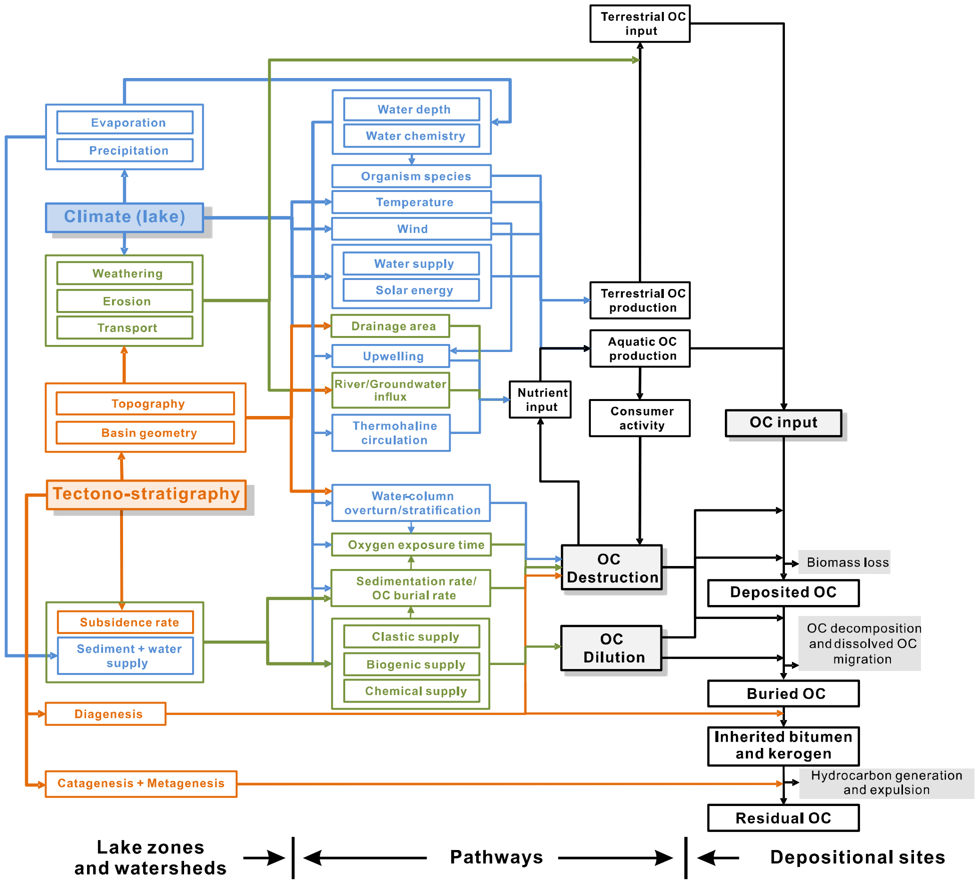

Figure 3 Click here to access/download;Figure;Figure 3.pdf

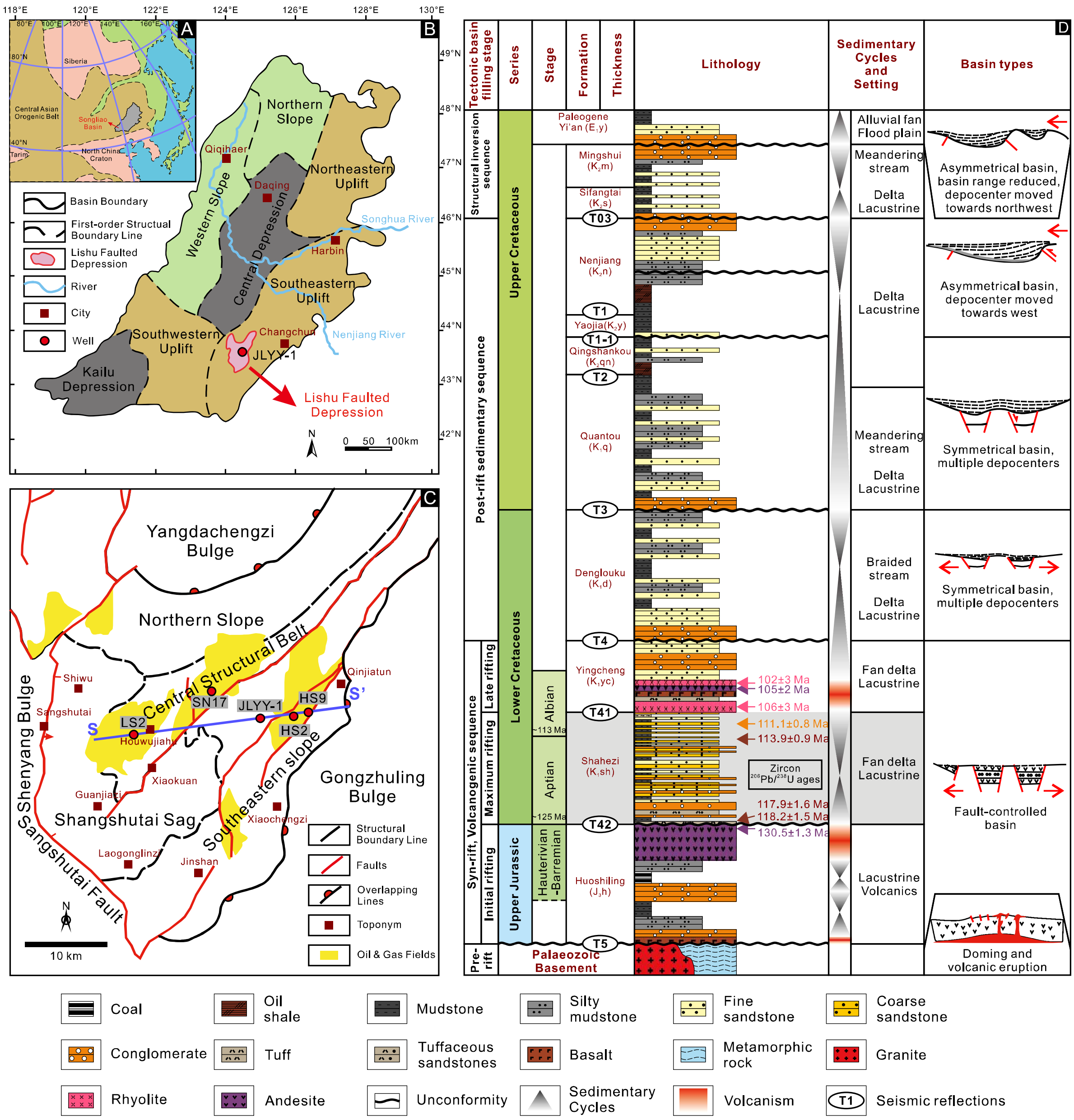

Figure 4

Click here to access/download;Figure;Figure 4.pdf

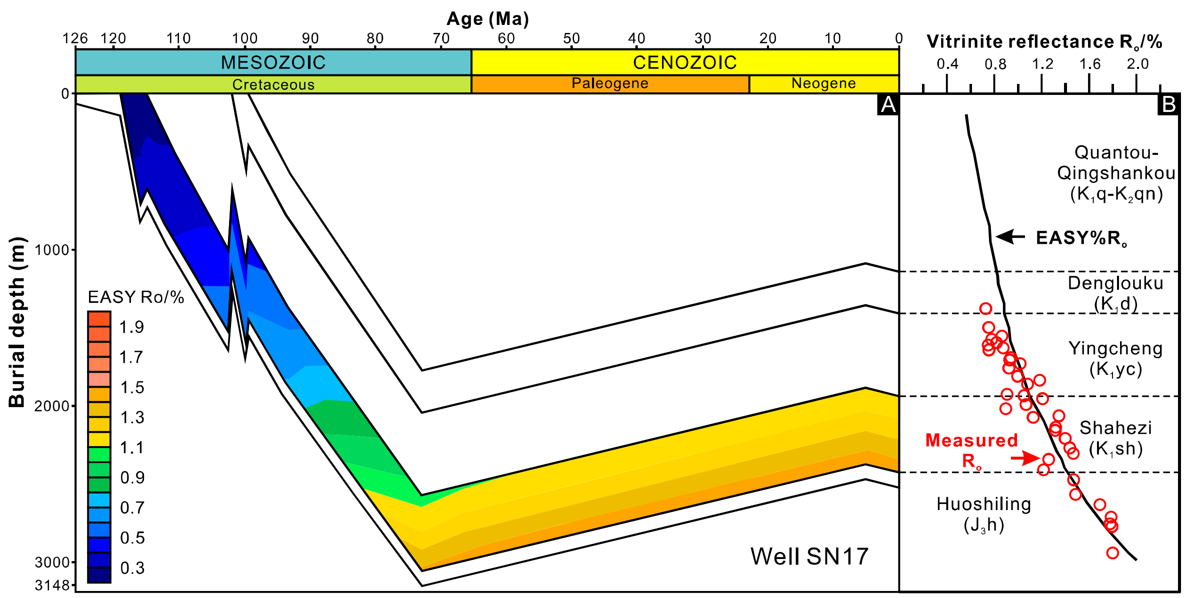

Figure 5

Click here to access/download;Figure;Figure 5.pdf

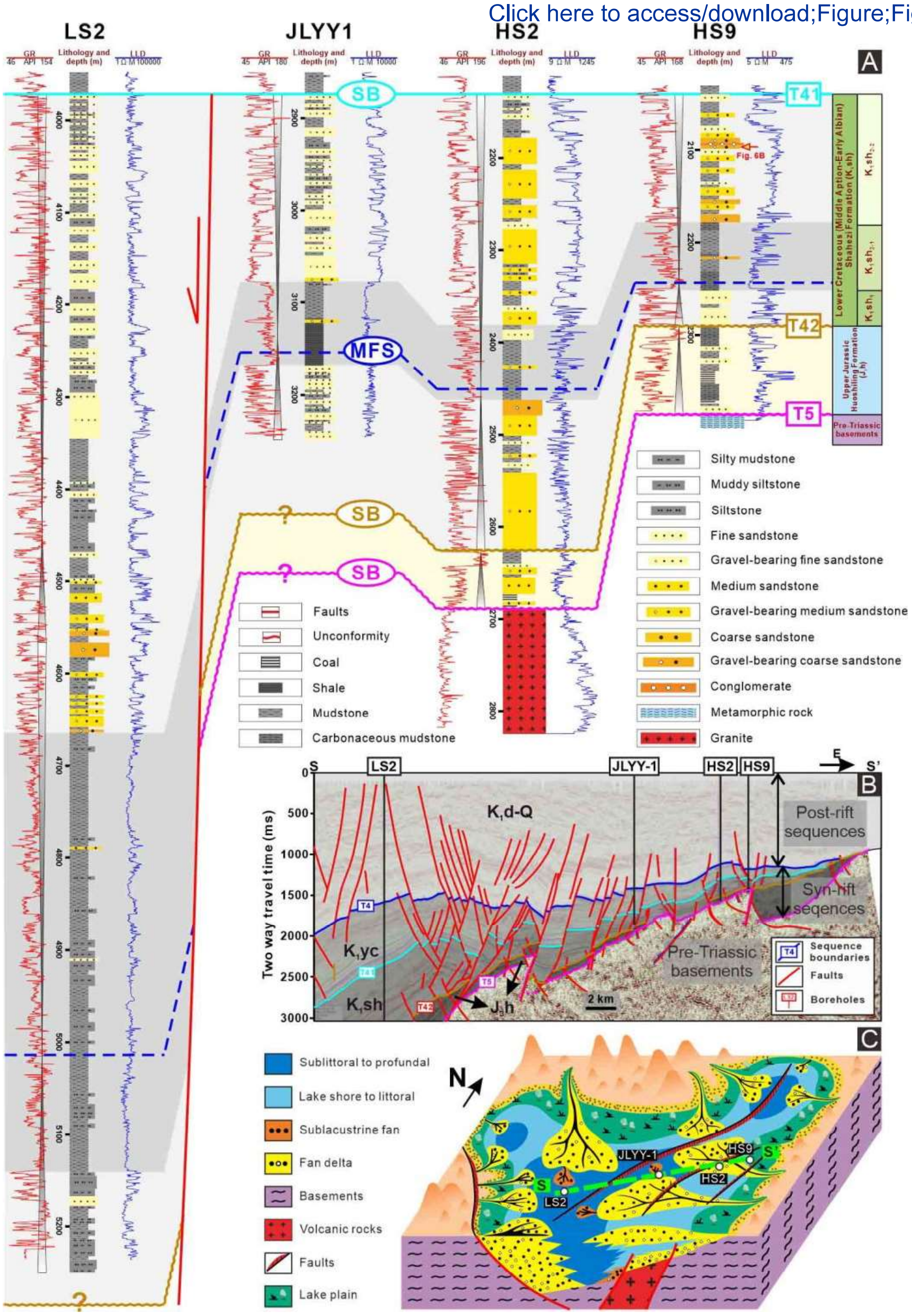

Figure 6 Click here to access/download;Figure;Figure 6.pdf

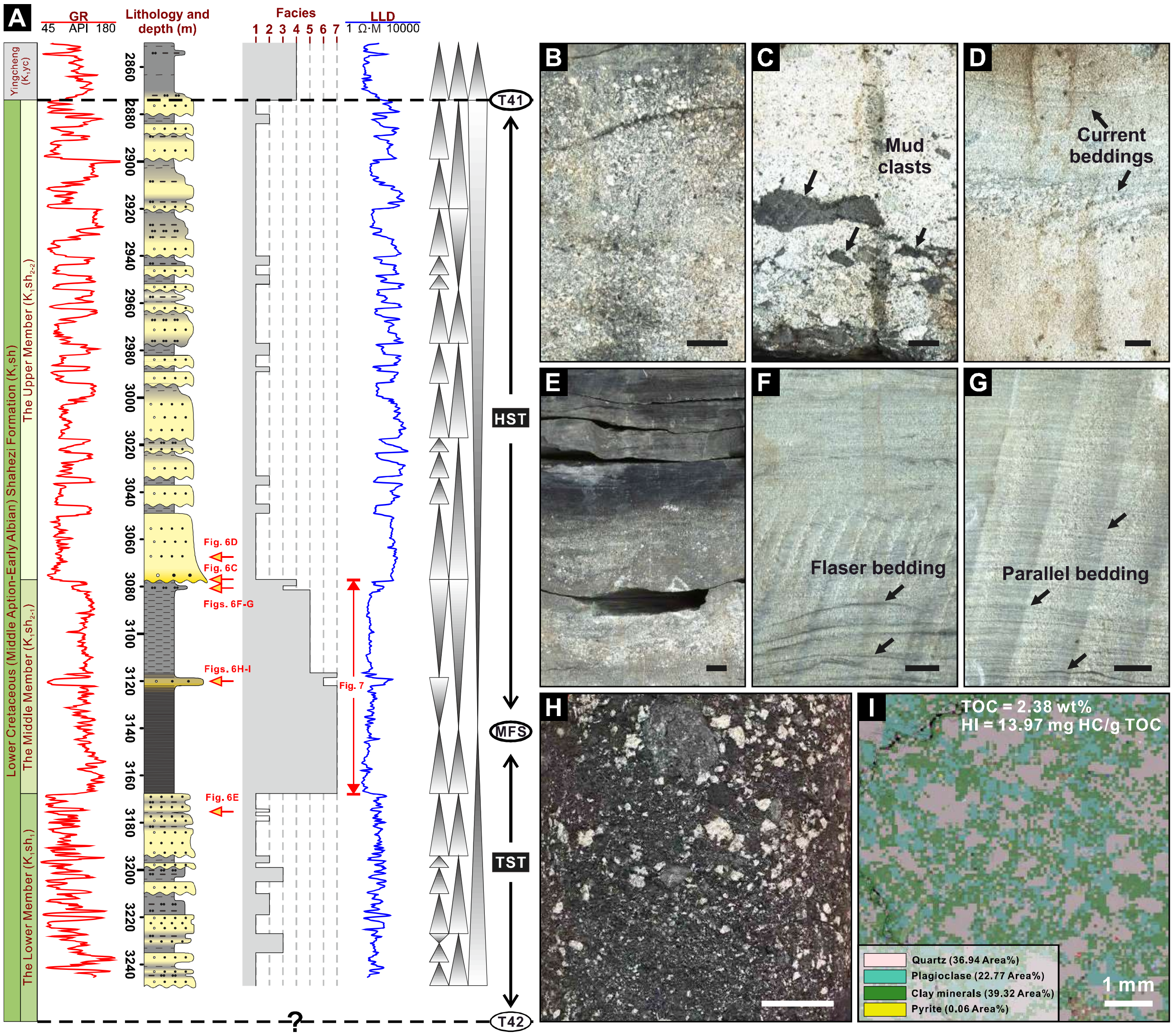

Figure 7

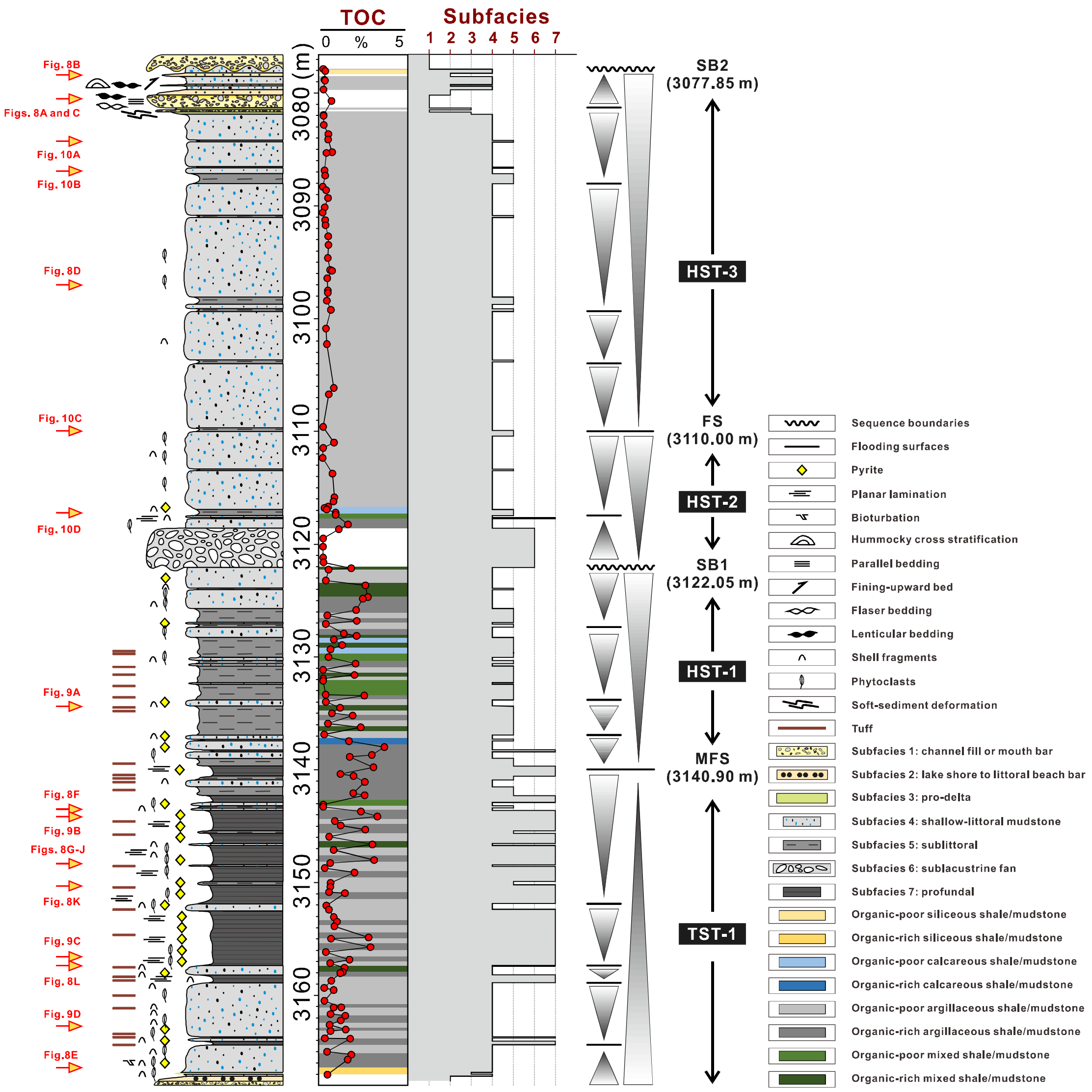

TOC
0 % 5
Subfacies
1 2 3 4 5 6 7
(m)
3080
3090
3100
3110
3120
3130
3140
3150
3160
Fig. 8B
Figs. 8A and C
Fig. 10A
Fig. 10B
Fig. 8D
Fig. 10C
Fig. 10D
Fig. 9A
Fig. 8F
Fig. 9B
Figs. 8G-J
Fig. 8K
Fig. 9C
Fig. 8L
Fig. 9D
Fig. 8E
SB2
(3077.85 m)
HST-3
FS
(3110.00 m)
HST-2
SB1
(3122.05 m)
HST-1
MFS
(3140.90 m)
TST-1
Sequence boundaries
Flooding surfaces
Pyrite
Planar lamination
Bioturbation
Hummocky cross stratification
Parallel bedding
Fining-upward bed
Flaser bedding
Lenticular bedding
Shell fragments
Phytoclasts
Soft-sediment deformation
Tuff
Subfacies 1: channel fill or mouth bar
Subfacies 2: lake shore to littoral beach bar
Subfacies 3: pro-delta
Subfacies 4: shallow-littoral mudstone
Subfacies 5: sublittoral
Subfacies 6: sublacustrine fan
Subfacies 7: profundal
Organic-poor siliceous shale/mudstone
Organic-rich siliceous shale/mudstone
Organic-poor calcareous shale/mudstone
Organic-rich calcareous shale/mudstone
Organic-poor argillaceous shale/mudstone
Organic-rich argillaceous shale/mudstone
Organic-poor mixed shale/mudstone
Organic-rich mixed shale/mudstone

Figure 8

Click here to access/download;Figure;Figure 8.pdf

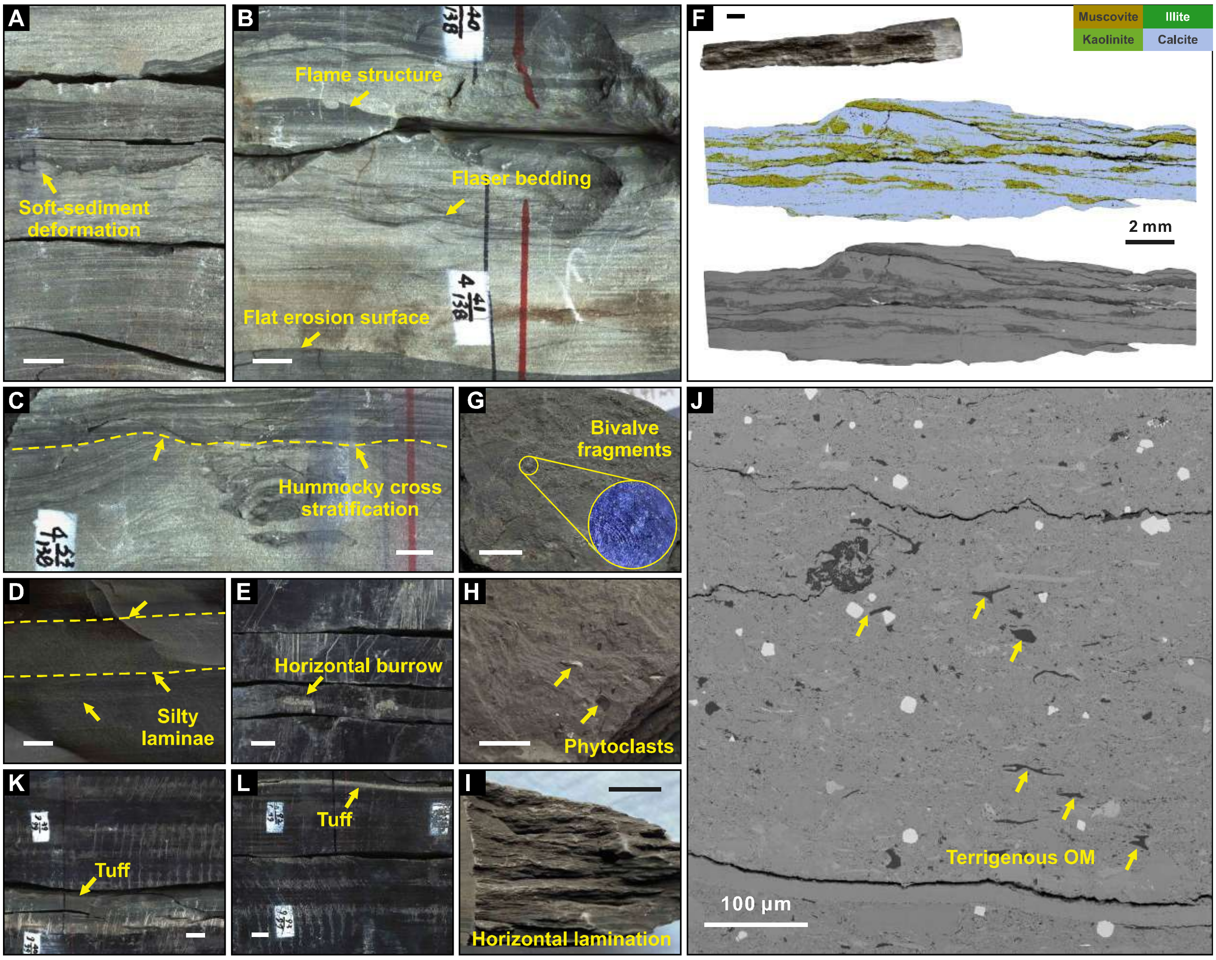

Figure 9

Click here to access/download;Figure;Figure 9.pdf

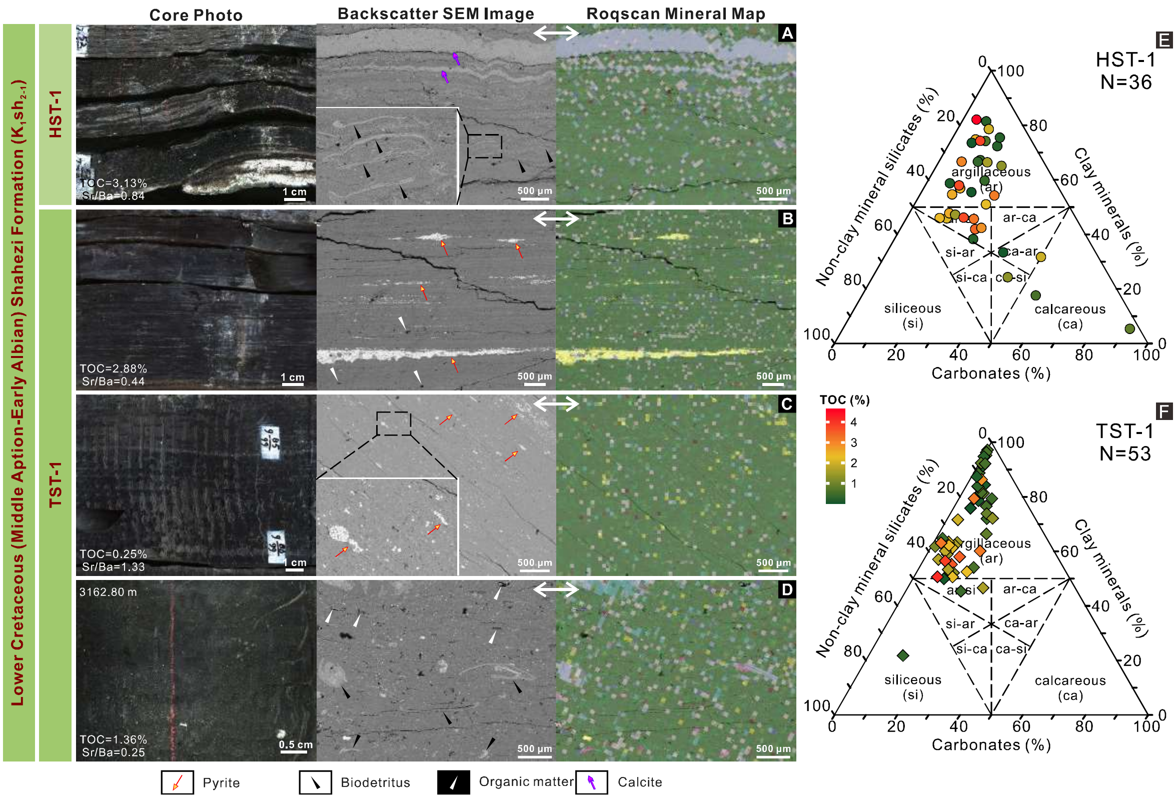

Figure 10

Click here to access/download;Figure;Figure 10.pdf

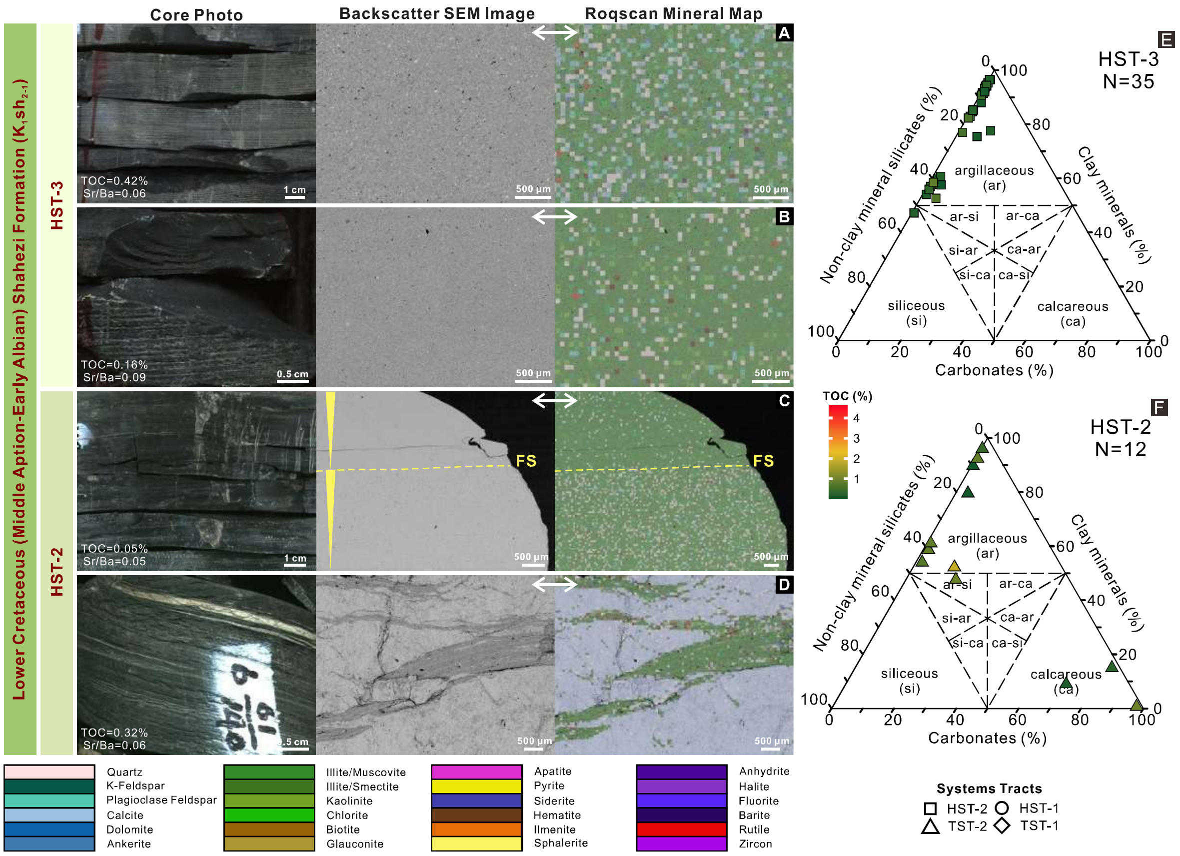

Figure 11

Click here to access/download;Figure;Figure 11.pdf

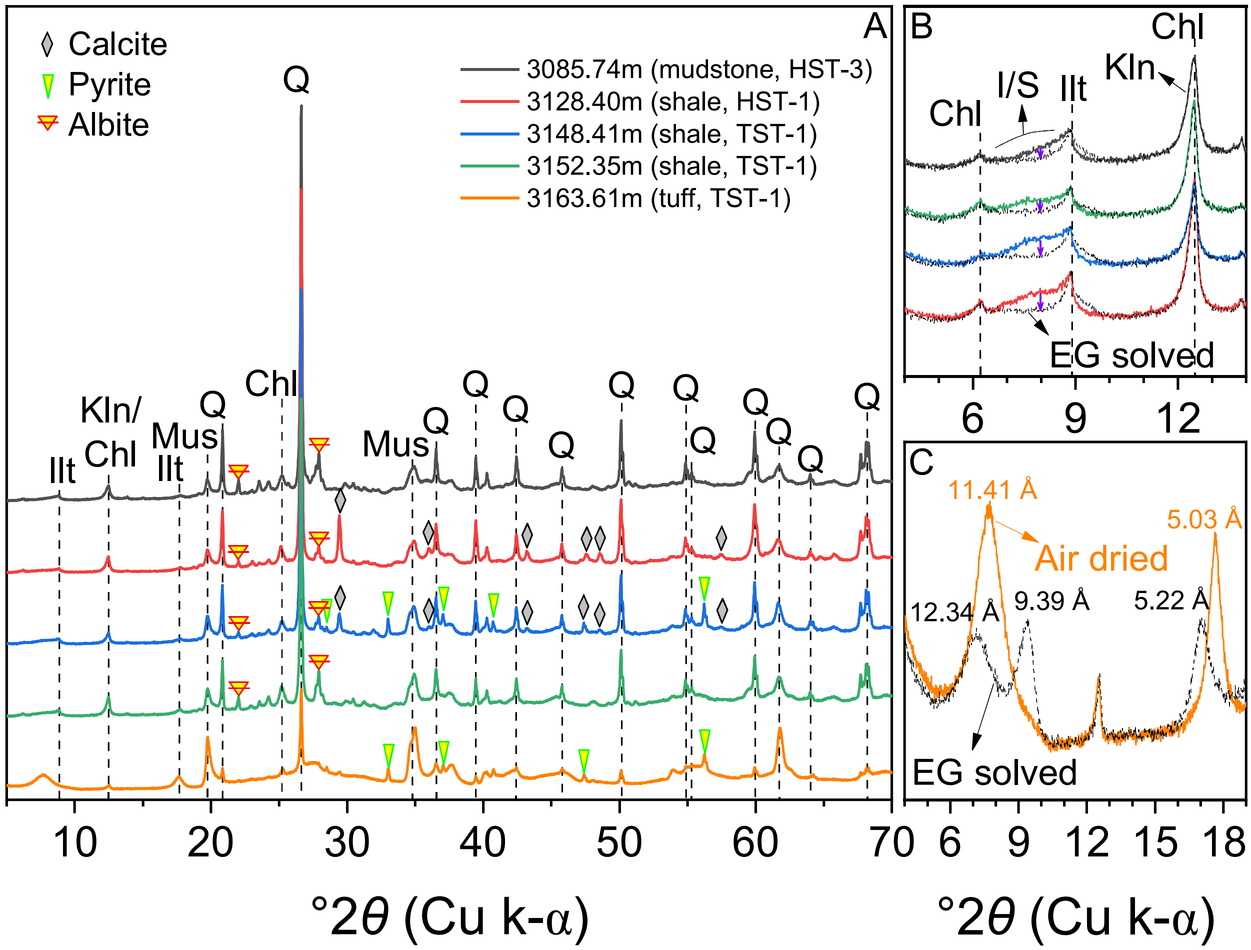

Figure 12

Click here to access/download;Figure;Figure 12.pdf

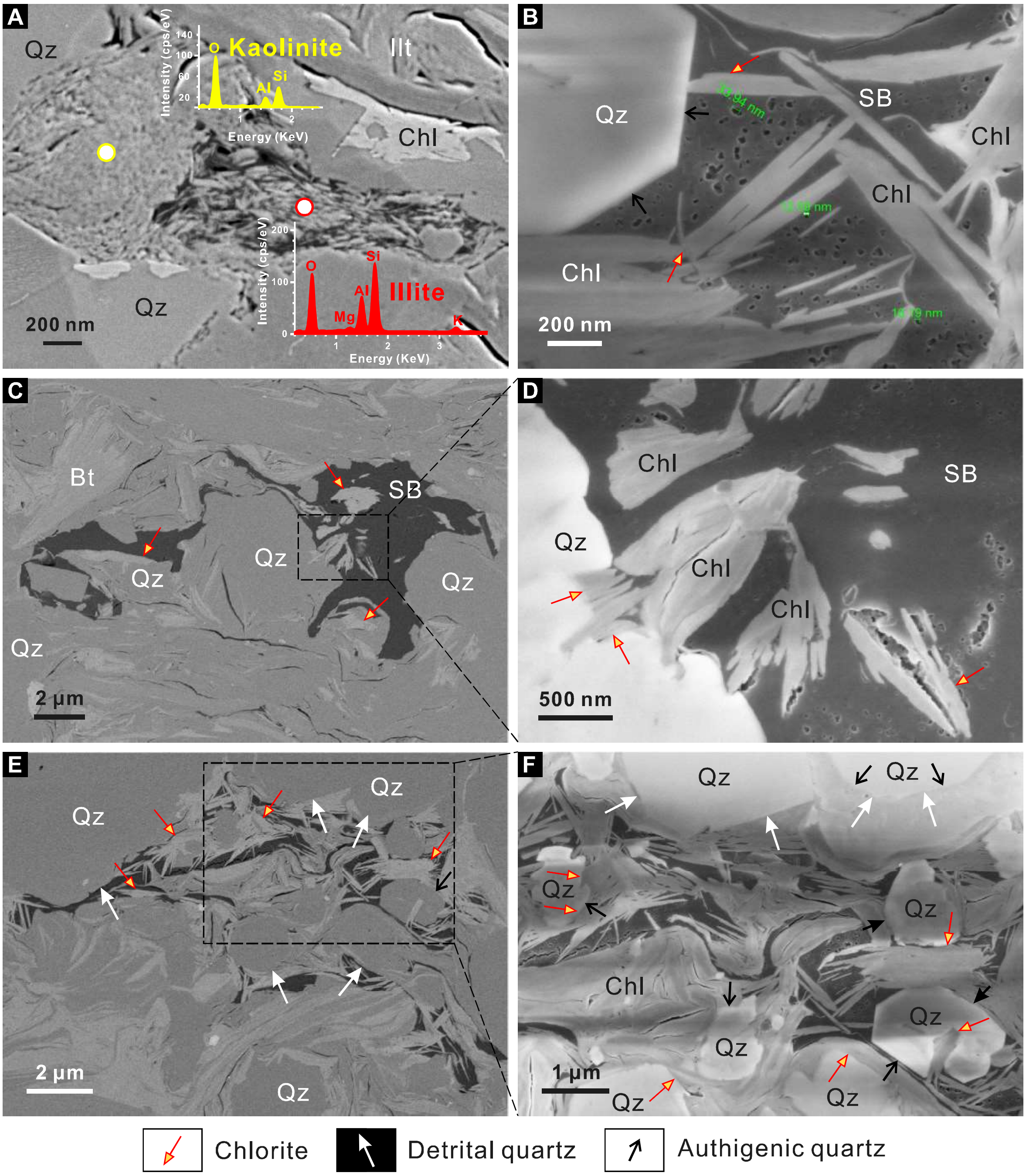

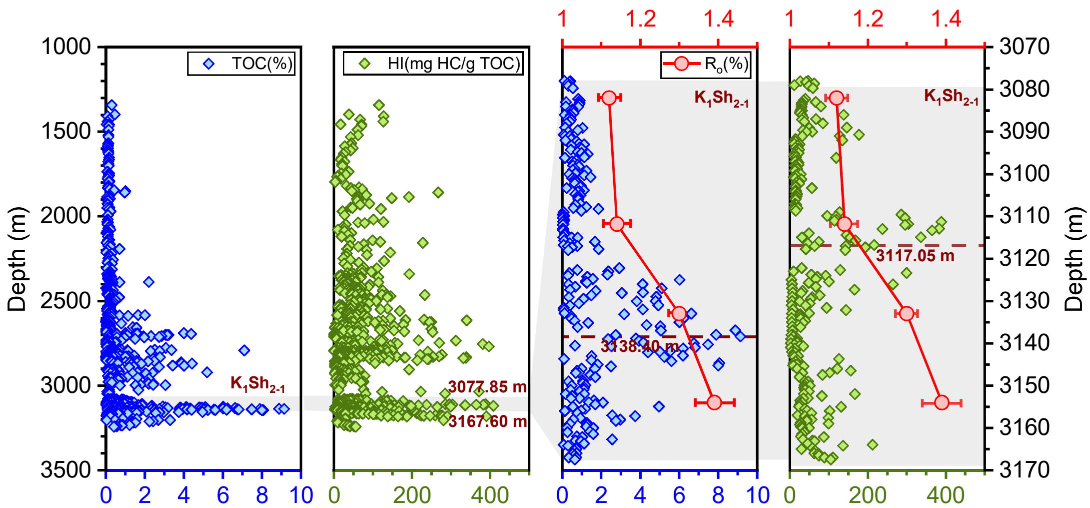
TOC(%)
HI(mg HC/g TOC)
R_o(%)
K_1Sh_{2-1}
3077.85 m
3167.60 m
3138.40 m
3117.05 m
Depth (m)
1000
1500
2000
2500
3000
3500
3070
3080
3090
3100
3110
3120
3130
3140
3150
3160
3170
0
2
4
6
8
10
200
400
1
1.2
1.4

Figure 14

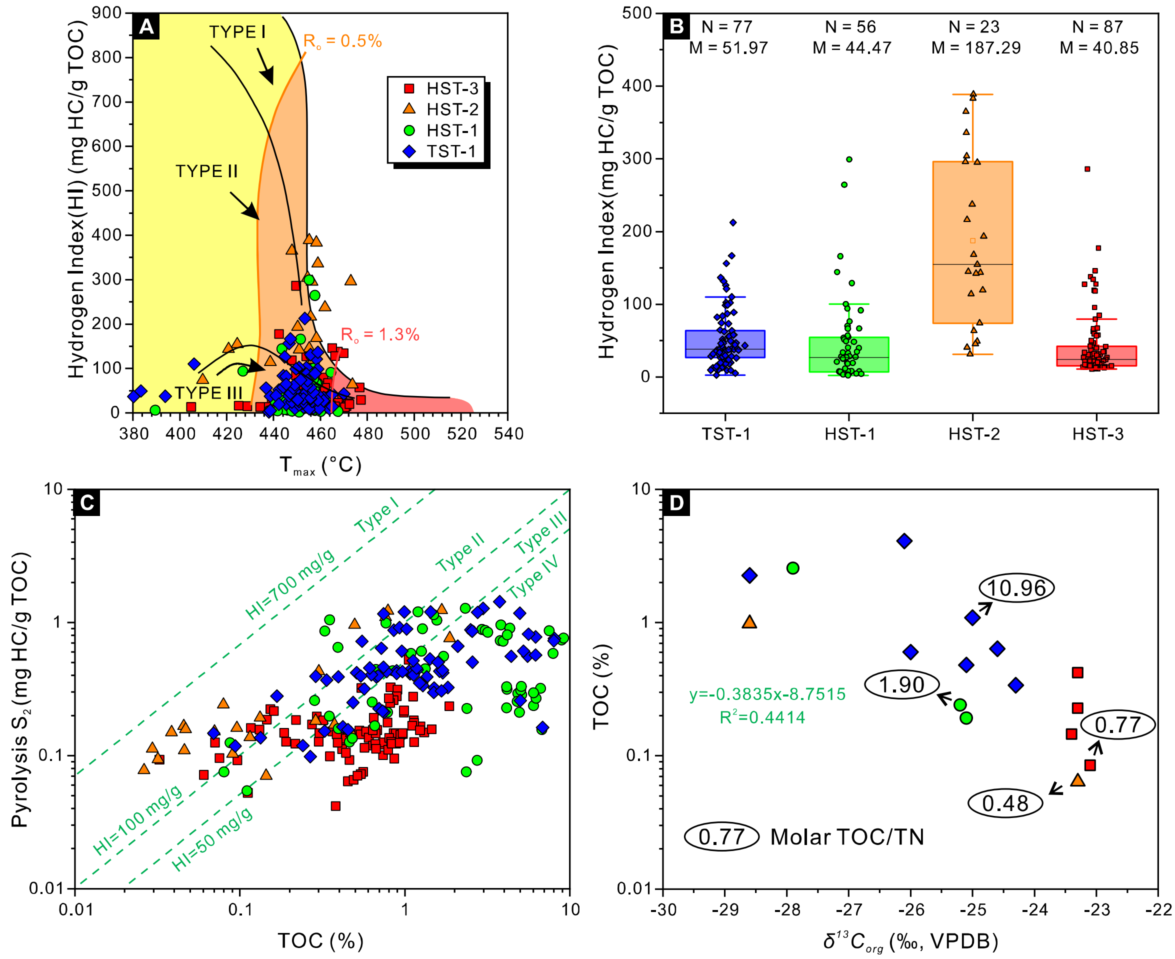
A
TYPE I
Ro = 0.5%
TYPE II
TYPE III
Ro = 1.3%
HST-3
HST-2
HST-1
TST-1
Hydrogen Index(HI) (mg HC/g TOC)
Tmax (°C)
B
N = 77
M = 51.97
N = 56
M = 44.47
N = 23
M = 187.29
N = 87
M = 40.85
Hydrogen Index(mg HC/g TOC)
TST-1
HST-1
HST-2
HST-3
C
Type I
Type II
Type III
Type IV
HI=700 mg/g
HI=100 mg/g
HI=50 mg/g
Pyrolysis S2 (mg HC/g TOC)
TOC (%)
D
10.96
1.90
0.77
0.48
y=-0.3835x-8.7515
R²=0.4414
0.77 Molar TOC/TN
TOC (%)
δ13Corg (‰, VPDB)

Figure 15

Click here to access/download;Figure;Figure 15.pdf

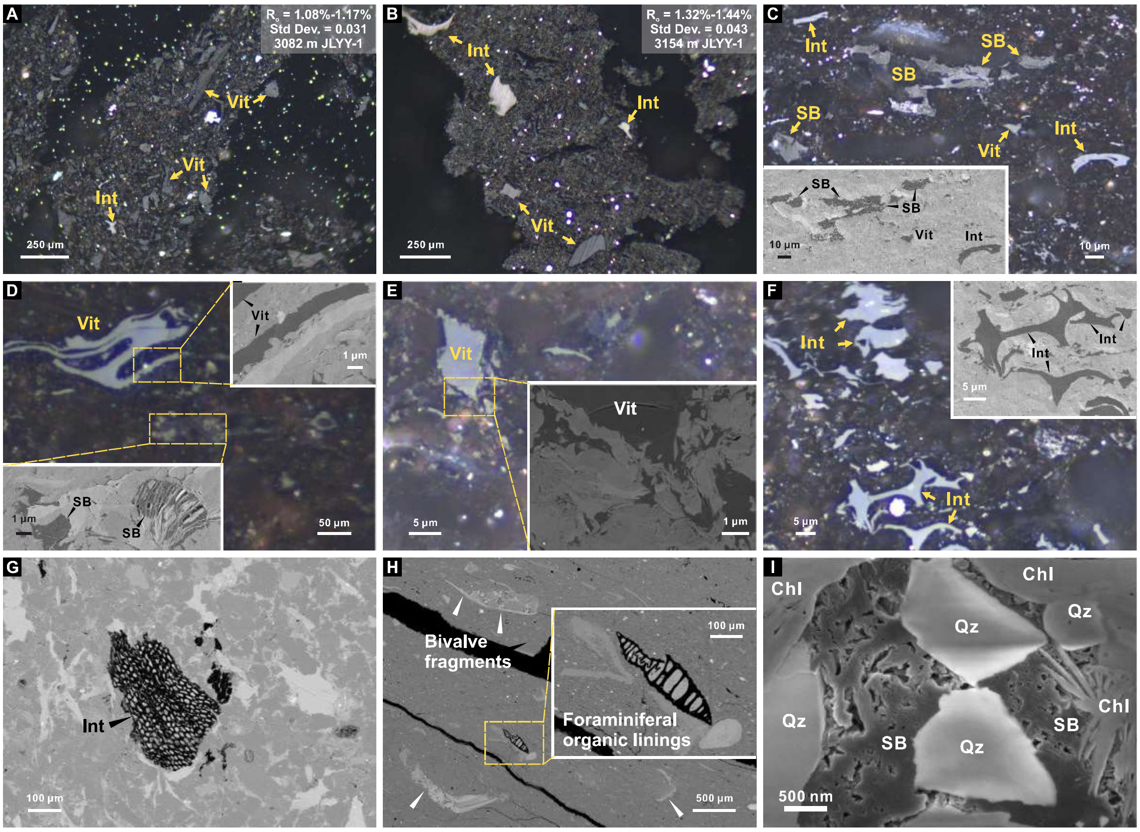

Figure 16

[Click here to access/download;Figure;Figure 16.pdf]

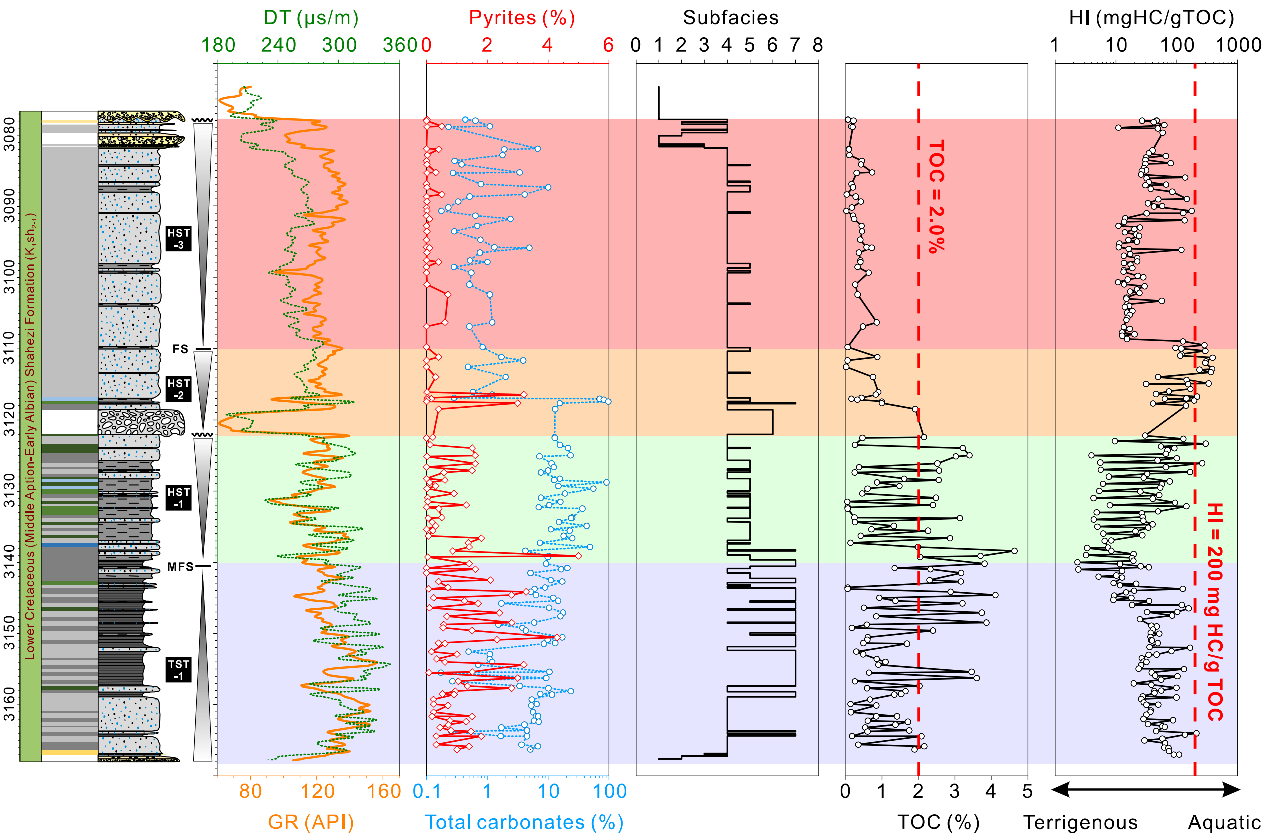

Figure 17

Click here to access/download;Figure;Figure 17.pdf

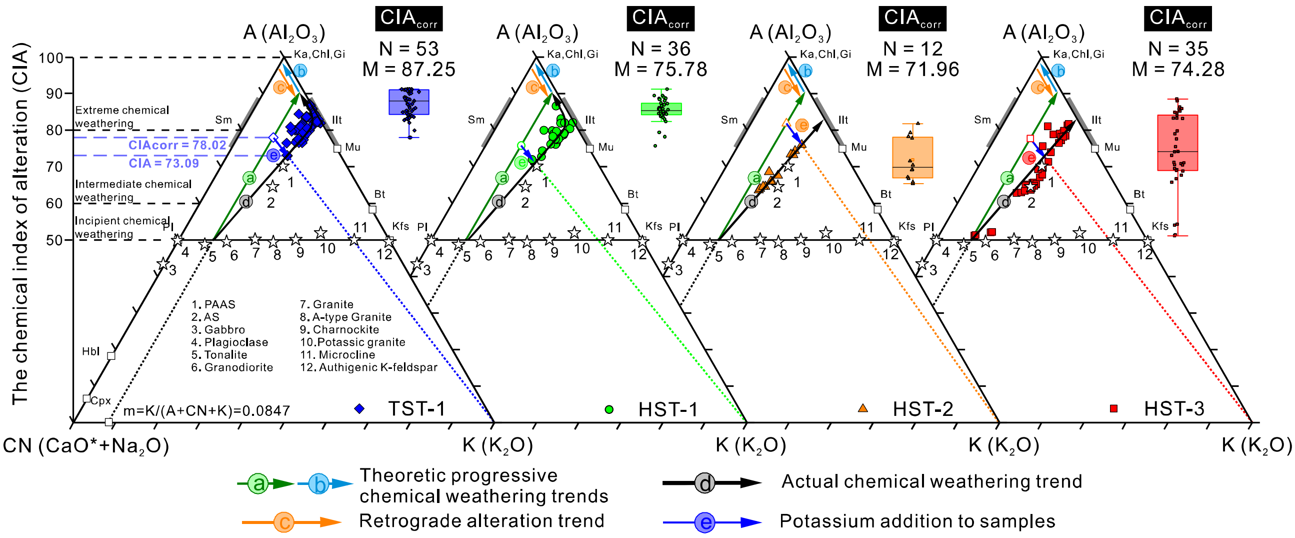

Figure 18

Click here to access/download;Figure;Figure 18.pdf

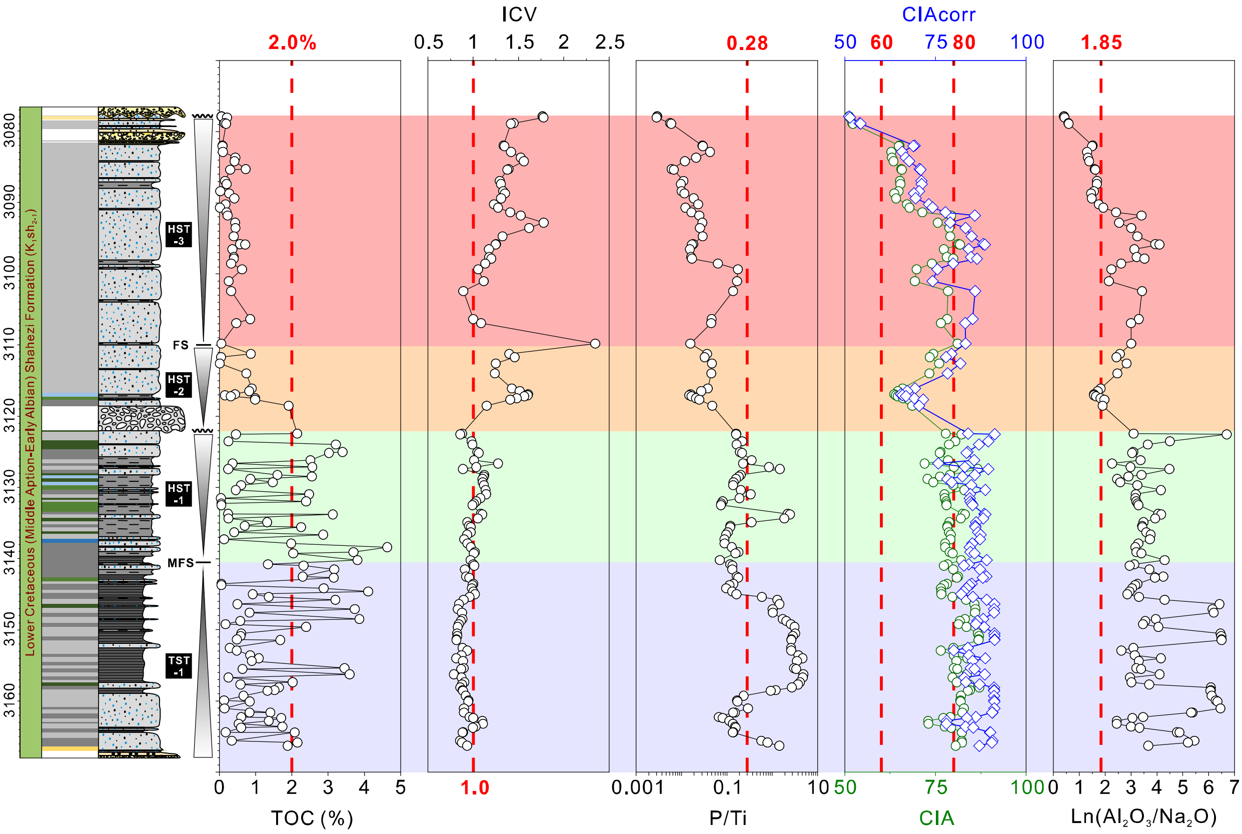

Figure 19 Click here to access/download;Figure;Figure 19.pdf

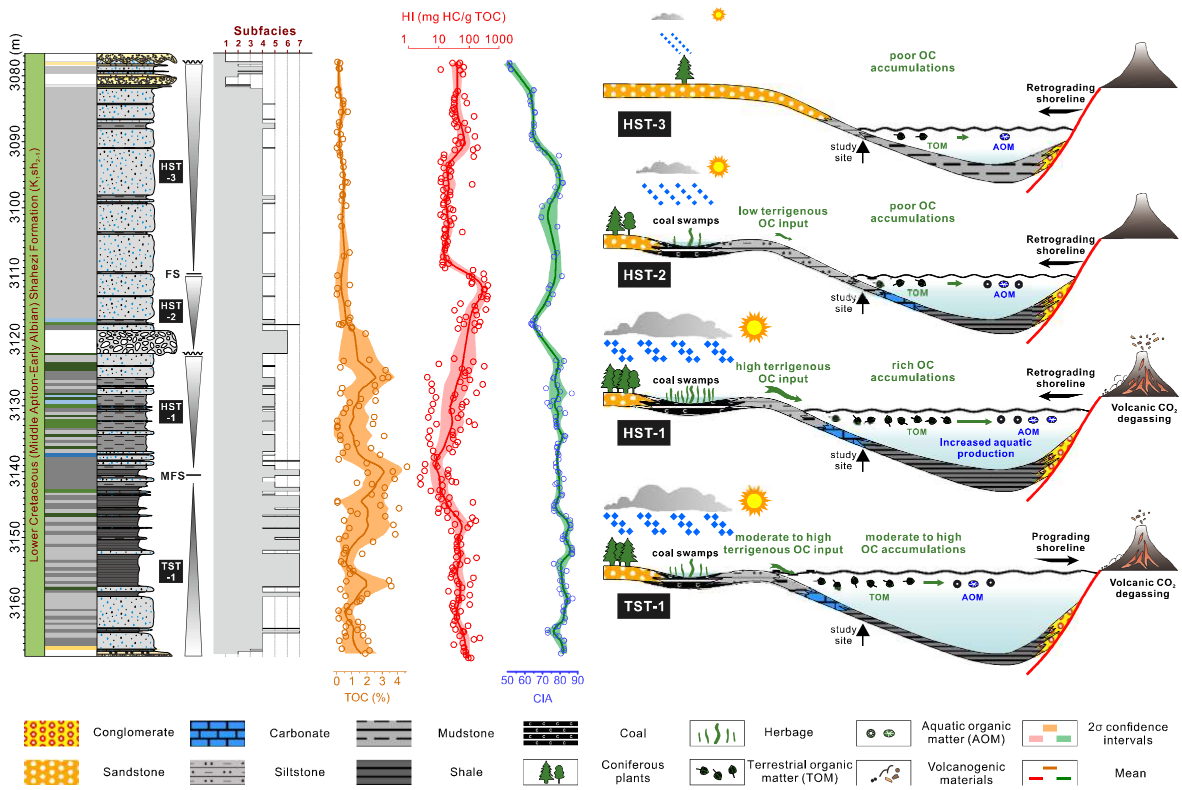

Figure 20 Click here to access/download;Figure;Figure 20.pdf

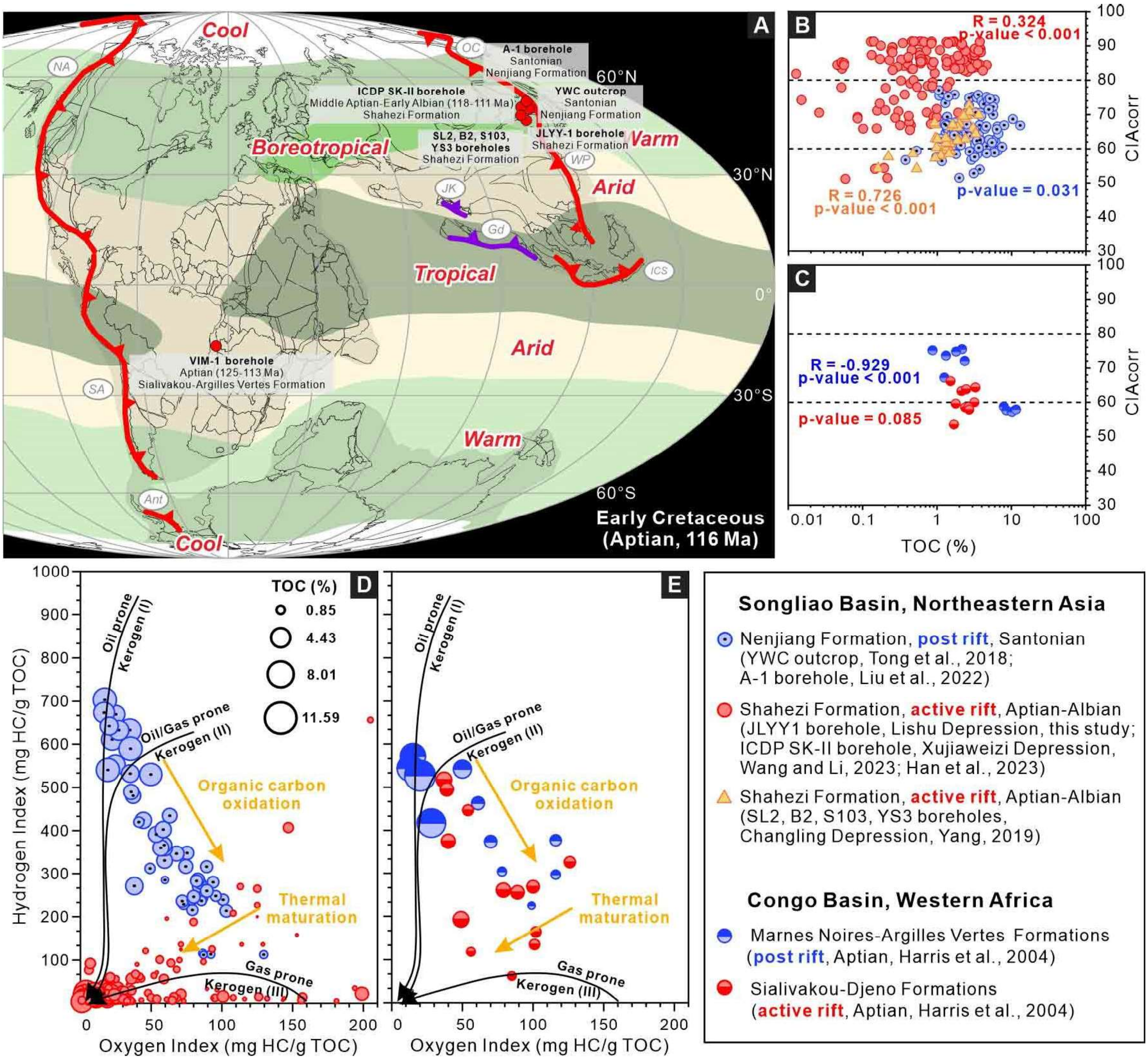

Table 1. The regions, basins, formations, ages, and data resources of organic shales and mudstones that have been reported to be dominated by gas-prone kerogens and deposited in global lacustrine settings.

Region	Basin/ Lake	Formation	Age	Thermal maturity	TOC/%	Hydrogen Index /(mgHC/gTOC)	Oxygen Index /(mgHC/gTOC)	Vitrinite+ Inertinite (%)	References
East Africa	Albert	-	Quaternary	immature	2.92% in average	~25–550	~20–180	-	Katz, 1990
NE Asia	Songliao	Shahezi	Early Cretaceous	R_o = 1.44%–2.10%	0.90%–3.60%	54.3–231.1	-	> 94%	Gao et al., 2018;
East Asia	Fuxin	Fuxin	Early Cretaceous	T_{max} = 426℃–463℃	0.05%–4.76%	34.30–360.99	-	-	Xu et al., 2022
West Africa	Mamfe	Mamfe	Early Cretaceous	R_o = 0.60%–0.82%	0.2%–2.5%	10–281	5–349	> 91.2%	Ndip et al., 2019
West Africa	Yola	Bima	Early Cretaceous	R_o = 1.12%–2.32%	0.41%–0.86%	24–127	-	-	Sarki Yandoka et al., 2017
South America	Ceará	Mundaú	Early Cretaceous	T_{max} = 437℃–463℃	0.6%–5.2%	20–600	-	-	Souza et al., 2021
North America	Richmond	-	Upper Triassic	mature and highly mature	-	< 300	< 100	-	Katz, 1995
SW China	Sichuan	Xujiahe	Upper Triassic	Ro = 0.74%–2.10%	0.61%–3.87%	6.93–168.35	-	47.31%–100%	Yang et al., 2019
South America	Cuyana	Agua de la Zorra	Triassic	T_{max} = 319℃–482℃	0.03%–4.65%	3.7–333.3	14.66–1333.3	-	Pedernera et al., 2021
Australia	Gunnedah	Snake Creek–Digby	Triassic	-	1%–14%	-	-	> 60%	Smyth and Mastalerz, 1991
East Africa	Nyasa	Snadd	Carboniferous /Permian	R_o = 0.62%–1.21%	0.4%–27.44%	0–232	4–28	> 80%	Kagya et al., 1991

Table 2. Units, computational formulae, and sources of geochemical indices used in this study.

Geochemical indices	Units	Equations for index calculation	Note	Sources
Pyrolyzed carbon (PC)	mg HC/g TOC	$PC = 0.083\times(S_0+S_1+S_2)$	Mass	Espitalié et al., 1984
Total organic carbon (TOC)	%	$TOC = RC^{1} + PC$	Mass	Espitalié et al., 1984
Hydrocarbon index (HI)	mg HC/g TOC	$HI = S_2/TOC\times100$	Mass	Tissot and Welte, 1984
Transformation ratio	-	$TR = S_1/(S_1+S_2)$	Mass	Tissot and Welte, 1984
$Ln(Al_2O_3/Na_2O)$	-	-	Molar	von Eynatten et al., 2003
Chemical index of alteration (CIA) [2]	-	$CIA = [Al_2O_3/(Al_2O_3+CaO^{*2}+Na_2O+K_2O)]\times100$	Molar	Fedo et al., 1995; McLennan, 1993; Nesbitt and Young, 1982
Corrected chemical index of alteration (CIA_{corr}) [3]	-	$CIA_{corr} = [Al_2O_3/(Al_2O_3+CaO^*+Na_2O+K_2O_{corr}{}^{3})]\times100$	Molar	Panahi and Young, 1997; Panahi et al., 2000
Index of compositional variability (ICV)	-	$ICV = (Fe_2O_3+K_2O_{corr}+Na_2O+CaO+MgO+MnO+TiO_2)/Al_2O_3$	Molar	Cox et al., 1995

[1] RC: the content of residual organic carbon after pyrolysis;

[2] CaO*: the corrected CaO values in silicate minerals;

[3] K_2O_{corr}: the corrected K_2O values with metasomatic K_2O addition removed.

Declaration of interests

☒The authors declare that they have no known competing financial interests or personal relationships that could have appeared to influence the work reported in this paper.

☐The authors declare the following financial interests/personal relationships which may be considered as potential competing interests: